THE QUEST–La SILLA AGN VARIABILITY SURVEY

RÉGIS CARTIER[1,2,3], PAULINA LIRA[2], PAOLO COPPI[4], PAULA SÁNCHEZ[2], PATRICIA ARÉVALO[5], FRANZ E. BAUER[6,1,7],
DAVID RABINOWITZ[4], ROBERT ZINN[4], RICARDO R. MUÑOZ[2], AND NICOLÁS MEZA[2]

[1] Millennium Institute of Astrophysics MAS, Nuncio Monseõr Sótero Sanz 100 Providencia, Santiago, Chile
[2] Departamento de Astronomía, Universidad de Chile, Casilla 36-D, Santiago, Chile
[3] School of Physics & Astronomy, University of Southampton, Southampton, Hampshire, SO17 1BJ, UK
[4] Department of Astronomy, Yale University, New Haven, CT 06520-8101, USA
[5] Instituto de Física y Astronomía, Facultad de Ciencias, Universidad de Valparaíso, Gran Bretaña 1111, Valparaíso, Chile
[6] Instituto de Astrofísica, Pontifícia Universidad Católica de Chile, Casilla 306, Santiago, Chile
[7] Space Institute, 4750 Walnut Street, Suite 205, Boulder, CO 80301, USA

ABSTRACT

We present the characterization and initial results from the QUEST–La Silla active galactic nucleus (AGN) variability survey. This is an effort to obtain well-sampled optical light curves in extragalactic fields with unique multiwavelength observations. We present photometry obtained from 2010 to 2012 in the XMM-COSMOS field, which was observed over 150 nights using the QUEST camera on the European Southern Observatory (ESO) Schmidt telescope. The survey uses a broadband filter, the Q band, similar to the union of the g and the r filters, achieving an intrinsic photometric dispersion of 0.05 mag and a systematic error of 0.05 mag in the zero point. Since some detectors of the camera show significant nonlinearity, we use a linear correlation to fit the zero points as a function of the instrumental magnitudes, thus obtaining a good correction to the nonlinear behavior of these detectors. We obtain good photometry to an equivalent limiting magnitude of $r \sim 20.5$. The astrometry has an internal precision of $\sim 0\rlap{.}''1$ and an overall accuracy of $0\rlap{.}''2$ when compared to the Sloan Digital Sky Survey. Studying the optical variability of X-ray-detected sources in the XMM-COSMOS field, we find that the survey is $\sim 75\%$–80% complete to magnitudes $r \sim 20$, and $\sim 67\%$ complete to a magnitude $r \sim 21$. Additionally, broad-line (BL) AGNs have larger variation amplitude than non-broad-line (NL) AGNs, with $\sim 80\%$ of the BL AGNs classified as variable, while only $\sim 21\%$ of the NL AGNs are classified as variable. We also find that $\sim 22\%$ of objects classified as galaxies (GALs) are also variable. The determination and parameterization of the structure function ($\mathrm{SF_{norm}}(\tau) = A\tau^{\gamma}$) of the variable sources show that most BL AGNs are characterized by $A > 0.1$ and $\gamma > 0.025$. It is further shown that NL AGNs and GAL sources occupying the same parameter space in A and γ are very likely to correspond to obscured or low-luminosity AGNs. Our samples are, however, small, and we expect to revisit these results using larger samples with longer light curves obtained as part of our ongoing survey.

Key words: astrometry – quasars: general – techniques: photometric

1. INTRODUCTION

Despite the fact that variability is one of the defining characteristics of active galactic nuclei (AGNs), we do not completely understand the mechanisms that drive such variation. Our understanding misses significant details of how AGN variability at different wavelengths is related (see, e.g., Arévalo et al. 2008, 2009; Lira et al. 2011, 2015) and how physical properties of the central engine (e.g., luminosity, black hole mass, hardness ratio [HR], optical colors) are related to well-defined variability properties of the system (e.g., characteristic timescale, variability amplitude). From a cosmological perspective, the strong evolution of AGNs opens the possibility to observe changes of the structure and feeding of AGNs over cosmic time (see Shemmer et al. 2014, and references therein). In fact, controversy remains regarding the redshift dependence of AGN variability, since the observed wavelength and the minimum luminosity in a sample are highly correlated with redshift (see Vanden Berk et al. 2004; Kelly et al. 2009; MacLeod et al. 2010; Morganson et al. 2014, and references therein). Finally, the property of being highly variable makes AGN selection by variability a very promising tool to find them.

To study in detail the variability properties of individual AGNs and to use this information to rule out different variability models, it is necessary to probe a wide range of timescales. Hence, long and intense campaigns are crucial. Fortunately, in recent years, surveys covering a significant part of the sky, revisiting the same regions on timescales from days to years, and containing a large sample of serendipitous objects —blind surveys—are now becoming available as predecessors of the Large Synoptic Survey Telescope (LSST; Ivezić et al. 2008). LSST will revisit each part of the southern sky ($\delta_{J2000} < +34.5$) approximately every three nights over 10 years and will observe in six bands ($ugrizy$) to a limiting magnitude of $r \simeq 24.5$ mag. Among the LSST predecessors we have the following: The Sloan Digital Sky Survey (SDSS; York et al. 2000) equatorial Stripe-82 covers roughly 280 deg^2 in the 20^h34^m–04^h08^m R.A. range and decl. $|\delta_{J2000}| < 1\rlap{.}°266$ (Ivezić et al. 2007; Sesar et al. 2007). This region was observed in five bands ($ugriz$) one to three times a year from 2000 to 2005 (SDSS-I), and then from 2005 to 2008 at an increased cadence of 10–20 times per year as part of the SDSS-II supernova survey (Frieman et al. 2008). The Catalina Real-time Transient Survey (CRTS; Drake et al. 2009; Graham et al. 2014) covers $-75° < \delta_{J2000} < 75°$, observing in the V filter to a limiting magnitude of ~ 19–21.5 (depending on the telescope used). CRTS covers a total of 33,000 deg^2 observing up to ~ 2500 deg^2 per night, with four exposures per visit, separated by 10 minutes, over 21 nights per lunation (i.e., revisiting a field every 10–15 days). The Palomar Transient Factory (Law

et al. 2009; Rau et al. 2009) covers $-15° < \delta_{J2000} < 85°$ using two broad bandpasses, namely, the Mould R band and g band, to a limiting magnitude of $R \simeq 21.0$ mag and $g \simeq 21.6$ mag with a cadence of 3–5 days. The Panoramic Survey Telescope and Rapid Response System (Hodapp et al. 2004; Tonry et al. 2012) cover the entire northern sky down to $\delta \simeq -30°$ in six bands (g_p, r_p, i_p, z_p, y_p, and w_p; Tonry et al. 2012) to a limiting magnitude between 22.0 and 24.0 mag depending on the filter, revisiting a field every 4–5 days. Finally, the Dark Energy Survey (Abbott et al. 2005) is observing part of the southern sky in four bands ($griz$) to a limiting magnitude of $r \simeq 24$ mag, performing a roughly 30 deg^2 time domain survey for supernovae revisiting a field every few days (4–5 days).

One of the advantages of the QUEST–La Silla AGN Survey over these surveys is the very intense monitoring, observing the survey fields every possible night (although with large observing gaps from 2010 to 2012; see more details in Section 3 below). We obtain between two and five observations per night to remove spurious variability due to artifacts, to potentially study intranight AGN variability, and to produce stacked images to reach deeper magnitudes. Individual images reach a limiting magnitude between $r \sim 20.5$ mag and $r \sim 21.5$ mag for an exposure time of 60 or 180 s, respectively. One of the main characteristics of the QUEST–La Silla AGN Survey is that it is focused on deeply observed extragalactic fields with multiwavelength coverage, having nearly simultaneous observations in the near-infrared (near-IR) performed by the Visible and Infrared Survey Telescope for Astronomy (VISTA) surveys (see Section 3 below).

X-ray variability studies indicate that the X-ray short-timescale normalization of the power spectrum density (PSD) is correlated with the black hole mass (see McHardy 1988, 2013; Gierliński et al. 2008; Kelly et al. 2013), and also that the black hole mass is correlated with the break frequency (characteristic timescale) of the PSD (McHardy et al. 2006). These results have led to the suggestion that AGNs are scaled versions of Galactic X-ray binaries with supermassive black holes (McHardy et al. 2006), and that the X-ray characteristic timescale and the black hole mass are tightly related. Thus, AGN variability could be a robust black hole mass estimator for a significant number of AGNs if these relations can be extended to the optical/ultraviolet (UV) wavelengths. For a long time a significant anticorrelation between AGN variability amplitude and luminosity has been recognized in the optical/ UV regime (Uomoto et al. 1976; Hook et al. 1994; Trevese et al. 1994; Cristiani et al. 1997; Vanden Berk et al. 2004; Wilhite et al. 2008; MacLeod et al. 2010; Meusinger & Weiss 2013). Besides, some correlations between characteristic variability timescales and black hole mass have already been found (Collier & Peterson 2001; Kelly et al. 2009). Additionally, correlations between the optical variability amplitude and the black hole mass have been described (Wold et al. 2007; Wilhite et al. 2008; Kelly et al. 2009; MacLeod et al. 2010; Meusinger & Weiss 2013). However, these results seem to point toward a more fundamental inverse relation between the AGN variability amplitude, at timescales longer than 1 year, and the Eddington ratio (or accretion rate; Wilhite et al. 2008; Ai et al. 2010; MacLeod et al. 2010; Zuo et al. 2012; Meusinger & Weiss 2013). Further results indicate that AGN variability properties (e.g., the structure function) seem to change with other properties such as X-ray luminosity and radio loudness (see Vanden Berk et al. 2004; MacLeod

et al. 2010, and references therein). All these results naturally lead to the conclusion that AGN variability is intrinsically related to the physical parameters that govern the accretion in AGNs, and therefore variability studies using large samples are crucial to improve our understanding of the accretion process.

One of the reasons why these relations are not commonly used to estimate physical parameters is that until recently the sample of objects with good optical/UV/X-ray monitoring, having the required cadence of observations to probe the necessary timescales (up to years), was small. For example, the studies of Wold et al. (2007) and Kelly et al. (2009) were based on samples of only $\sim$100 AGNs. Larger variability studies, on the other hand, have been based on spectroscopically identified AGNs on the Stripe-82 (Wilhite et al. 2008; Ai et al. 2010; MacLeod et al. 2010; Schmidt et al. 2010; Butler & Bloom 2011), which have $\sim$60 photometric observations over a decade or on ensemble AGN studies with few observations (Vanden Berk et al. 2004). Since early AGN monitoring was mainly biased toward bright, color-selected, or highly variable sources, the calibration of the aforementioned relations is usually not representative of the whole AGN population. It would also be highly desirable to compare black hole mass estimations obtained using different methods to assess systematic uncertainties (e.g., traditional methods versus optical/X-ray variability black hole mass estimations). We expect to address most of these issues in the future using data collected as part of our survey.

Since most of the AGN bolometric luminosity is emitted in the UV/optical part of the spectrum and their spectral energy distribution (SED), this is the region of choice to carry out an AGN survey. However, the UV/optical region can be subject to strong obscuration. On the other hand, the X-rays—particularly hard X-rays—can pass through the obscuring material; thus, deep X-ray surveys provide a better census of the AGN population, particularly at low luminosities. X-ray observations are expensive, and therefore surveys at these energies are usually shallow or cover small areas. Clearly, to increase the synergy of any AGN variability survey, it is necessary to carry out intense optical monitoring in fields with extensive X-ray observations. This point is addressed in our survey by means of monitoring fields with extensive multi-wavelength coverage, ranging from the X-rays to the mid-IR, and spectroscopic follow-up.

Traditionally, the optical selection of AGNs has made use of the fact that AGNs show a UV excess in their SED compared to stars (see Schmidt & Green 1983). The UV-excess technique and the more recent selection methods based on optical colors (see Richards et al. 2002, 2009) are very efficient in finding AGNs in the regions of color space where the AGN density is higher than the density of stars or galaxies. However, these selection methods based on optical colors miss a significant fraction of AGNs with peculiar colors (e.g., red QSOs) or QSOs located at a redshift range ($2.5 \leqslant z \leqslant 3.0$) where their optical colors are similar to those of stars (see Fan 1999; Richards et al. 2002, 2009). On the other hand, the fact that AGNs are highly variable makes their selection by means of variability a very promising technique to find them regardless of their colors. This selection method has been successfully used to identify a large number of new QSO candidates (Kozłowski et al. 2010; Schmidt et al. 2010; Butler & Bloom 2011; MacLeod et al. 2011; Palanque-Delabrouille et al. 2011; Kim et al. 2012; Graham et al. 2014). Butler & Bloom (2011)

Table 1
Properties of the ESO 1 m Schmidt Telescope

Property	Value
Aperture diameter	1 m
Focal length	3.05 m
f-ratio	3.05
Plate scale	14.74 μm/″
Latitude of observatory	$-29°{:}15'$
Longitude of observatory	$70°{:}44'$
Elevation	2375 m

and Palanque-Delabrouille et al. (2011) have shown that selecting QSOs by their variability can increase considerably the number of QSO candidates in the redshift range where the colors of stars are similar to those of AGNs.

Since 2010 we have been carrying out an AGN variability survey using the wide-field QUEST camera located on the 1 m European Southern Observatory (ESO) Schmidt telescope at La Silla Observatory. The telescope was fully robotized by Yale University, and the QUEST camera was moved from the 48″ Palomar–Schimdt telescope to La Silla in 2009. The aims of our survey are (1) to test and improve variability selection methods of AGNs and find AGN populations missed by other optical selection techniques (see Schmidt et al. 2010; Butler & Bloom 2011; Palanque-Delabrouille et al. 2011); (2) to obtain a large number of well-sampled light curves, covering timescales ranging from days to years; and (3) to study the link between the variability properties (e.g., characteristic timescales and amplitude of variation and other parametric variability characterizations) and physical parameters of the system (e.g., black hole mass, luminosity, and Eddington ratio).

In this paper we present the technical description of our survey, and we study the relation of variability with multi-wavelength properties of X-ray-selected AGNs in the COS-MOS field. In Section 2, we summarize the characteristics of the ESO-Schmidt telescope and the QUEST camera and describe the operation of the robotic telescope. In Section 3, we present an overview of our observation fields, and we discuss the reasons that make them special for carrying out an AGN variability survey. In Section 4, we present the data reduction steps. In Section 5, we describe the steps to obtain the astrometric solution for the QUEST frames, and we present the quality of our astrometry. In Section 6, we define the Q-band photometric system and describe in detail the steps to obtain well-calibrated light curves, including a nonlinearity correction to the photometry. In Section 6, we also demonstrate the quality of our photometry, compare the quality of aperture and point-spread function (PSF) photometry, and present examples of our light curves. In Section 7 we study the relation of optical variability with multiwavelength properties of a sample of XMM-COSMOS X-ray-selected AGNs. In Section 8 we summarize our work and present our conclusions. A standard Λ cold dark matter cosmology with $H_0 = 70$ km s^{-1} Mpc^{-1}, $\Omega_M = 0.27$, and $\Omega_\Lambda = 0.73$ is assumed throughout the paper.

2. TELESCOPE AND CAMERA DESCRIPTION

Schmidt telescopes are the instrument of choice for large-area sky surveys because of their large field of view. The QUEST Camera was designed to operate at the 48″ Samuel Oschin Schmidt Telescope at the Palomar Observatory (see Baltay et al. 2007). Since 2009 the camera has been located in

Table 2
Properties of the QUEST Camera

| Property	Value
Number of CCDs	112
CCD pixel size	13 μm × 13 μm
Number of pixels per CCD	600 × 2400
Pixel size on sky	0″882 × 0″882
Array size, CCDs	4 × 28
Array size, pixels	9600 × 16,800
Array size, cm	19.3 cm × 25.0 cm
Array size on sky	3°6 × 4°6
Sensitive area	9.6 square degrees
Total pixels	161 × 10^6
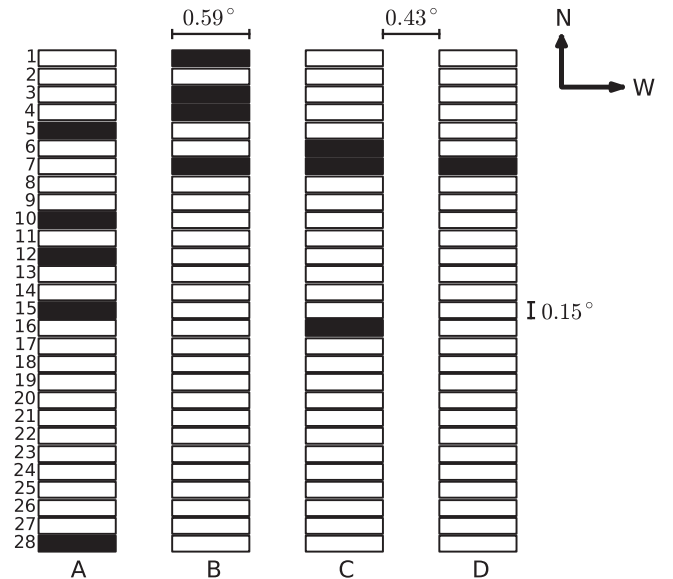
Figure 1. QUEST camera array; in black are shown dead CCDs. The camera consists of four "fingers" of 28 CCDs. The fingers are flagged as A, B, C, and D, and the columns from 1 to 28. The gaps between adjacent fingers are 0°43. Each CCD has 2400 × 600 pixels of 0°59 × 0°15.

the 1 m Schmidt telescope of the ESO at La Silla, Chile (see Table 1). This telescope is one of the largest Schmidt configurations in the Southern Hemisphere, situated in a dry site with dark skies and good seeing. Having a nearly identical optical configuration to the Palomar Schmidt, the QUEST camera was installed at La Silla without any changes to its front-end optics (Rabinowitz et al. 2012). The survey uses the Q-band filter described below (Section 6.1).

Telescope pointing and camera exposure are coordinated by a master scheduling program (Rabinowitz et al. 2012). A remote operator of one of the larger telescopes at the site (the ESO 3.6 m) decides when conditions are appropriate for opening the telescope and sends a remote command each night to enable the control software to open the dome. The control software automatically closes the dome whenever another nearby telescope (the 2.2 m) is closed, when the Sun rises, or when the remote operator sends a command to close. The remote operator can monitor and control the state of the Schmidt telescope via a Web-based interface.

The CCD camera is located at the prime focus of the telescope, about 3 m from the primary mirror. Its properties are summarized in Table 2. The camera consists of 112 CCDs arranged in four rows or "fingers" of 28 CCDs each, as shown in Figure 1, and
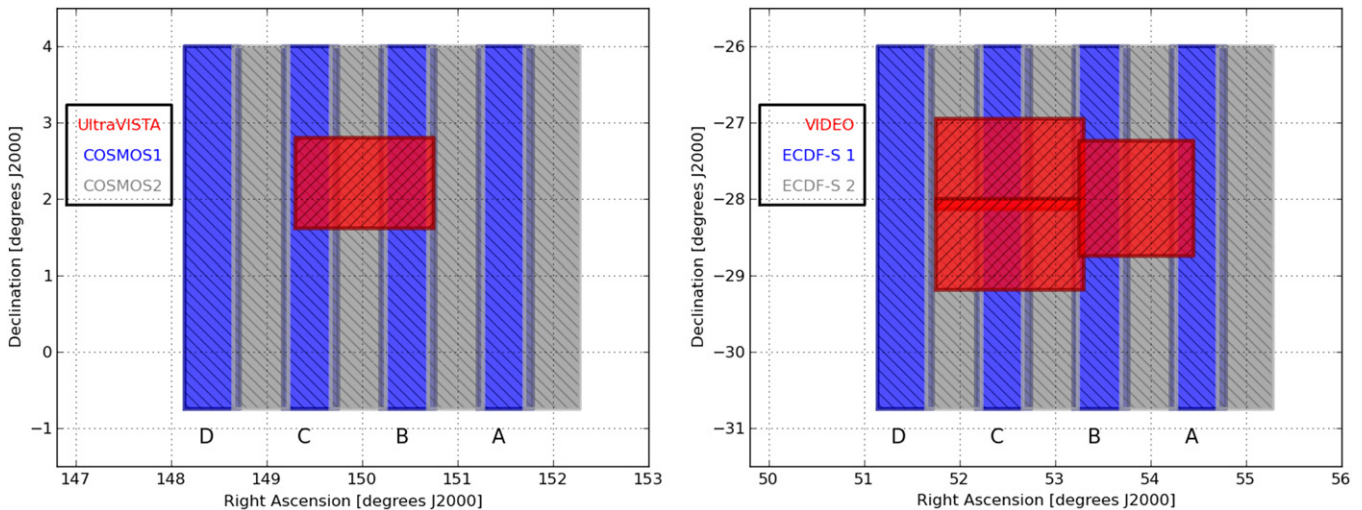
Figure 2. Observing layout for the COSMOS (left) and ECDF-S (right) fields. In blue is shown COSMOS1 and ECDF-S1 (first tile) and in gray COSMOS2 and ECDF-S 2 (second tile). The second tiles are displaced by half a degree from the first tiles. In red we show the area repeatedly observed by ultraVISTA and VIDEO in the COSMOS and ECDF-S fields, respectively. We flag the position of the four (A, B, C, and D) fingers for the first tiles.

covers $4°6 \times 3°6$ (north–south by east–west) on the sky. The fingers are flagged A, B, C, and D, and the columns of CCDs from 1 to 28. The gaps between the active areas of the CCDs in a row are typically 1 mm, and the gaps between the active areas in adjacent "fingers" are typically 22.8 mm, corresponding to $25'.8$. Each CCD has 600×2400 pixels of $13 \ \mu$m $\times$ $13 \ \mu$m in size and a pixel scale of $0''.882 \ \mathrm{pixel}^{-1}$. Therefore, to obtain a full coverage of the $4°6 \times 3°6$ field of view, it is necessary to displace the telescope by half a degree in R.A. to obtain an image pair made of two tiles (see Figure 2).

Several CCDs have areas of high dark current owing to defective, electron-emitting pixels in the CCD substructure or to a bad readout amplifier. By subtracting dark calibration images, the unfavorable influence of these defects on source detection is largely eliminated. However, about 16% of the CCDs are useless because they are permanently off, randomly turn on and off, or have large defective areas that make it impossible to obtain an acceptable PSF, all of which hamper the astrometric solution owing to the low number of stars detected and fake detections. The effective sky area covered by the functioning CCDs is $\sim$7.5 deg^2.

3. SURVEY FIELDS

We carried out the AGN variability survey observing the COSMOS, ECDF-S, ELAIS-S1, XMM-LSS, and Stripe-82 fields. These fields were chosen as a result of the wealth of ancillary data available for them, including *XMM-Newton*, *Chandra*, *GALEX*, *HST*, *Herschel*, *Spitzer*, and ground-based photometry and spectroscopy.

Additionally, the COSMOS, ECDF-S, ELAIS-S1, and XMM-LSS fields have been repeatedly observed in the near-IR since 2009, as part of the VISTA public surveys UltraVISTA (McCracken et al. 2012) and VIDEO (Jarvis et al. 2013). The aims of these VISTA surveys are to study the evolution of galaxies out to $z \sim 4$ and achieve a comprehensive view of AGNs and the most massive galaxies up to the epoch of reionization. UltraVISTA observations were carried out over the same period as our survey, and an article presenting the study of the AGN near-IR light curves is under way (P. Sánchez et al., 2015 in preparation).

The equatorial Stripe-82 is particularly valuable for variability studies (see Sesar et al. 2007). This region has been repeatedly observed as part of the SDSS since 1998; this will allow us to extend light curves of some of the Stripe-82 AGNs, combining SDSS and QUEST photometry over more than 15 years.

In Figures 2 and 3 we show the layout used to cover the COSMOS, ECDF-S, ELAIS-S1, and XMM-LSS fields. For the COSMOS, ECDF-S, ELAIS-S1, and Stripe-82 we used two tiles to cover the entire regions, whereas to cover the XMM-LSS field we used four tiles (see Figure 3).

A brief summary of the observations is as follows. In 2010 we obtained just a few observations for some fields ($\sim$20 nights). During 2011–2012, as a result of problems with the dome wheels of the telescope, we observed between 100 and 150 nights per field (twice per night). From 2013 onward the observations have been performed more regularly using an exposure time of 180 s (twice per night), reaching a magnitude limit of $Q \sim 20.5$ ($r \sim 21$), and observing each of our fields in more than 100 nights per year. Between 2011 March and the end of 2014 December we observed COSMOS on $\sim$370 nights, ECDF-S on $\sim$290 nights, ELAIS-S1 on $\sim$500 nights, Stripe-82 on $\sim$450 nights, and XMM-LSS on $\sim$360 nights. In the case of XMM-LSS we usually observed two tiles per night, either tile 1 and tile 2 or tile 3 and tile 4. Observations of ECDF-S and XMM-LSS until 2012 have been reduced, while ELAIS-S1 and Stripe-82 are reduced until 2014. We expect to continue collecting data until mid-2016.

From Section 5 onward, the analysis presented corresponds to data obtained from 2010 to 2012 in the COSMOS field.

4. DATA REDUCTION

For a typical night we take darks of 10, 60, and 180 s, as well as morning and evening twilight flats. The exposure times for our science images are either 60 or 180 s, with two image pairs obtained per field per night. We reduce the QUEST data using our own custom IRAF[7] scripts that carry out the reduction steps described below.

---

[7] IRAF is distributed by the National Optical Astronomy Observatories, which are operated by the Association of Universities for Research in Astronomy, Inc., under cooperative agreement with the National Science Foundation.
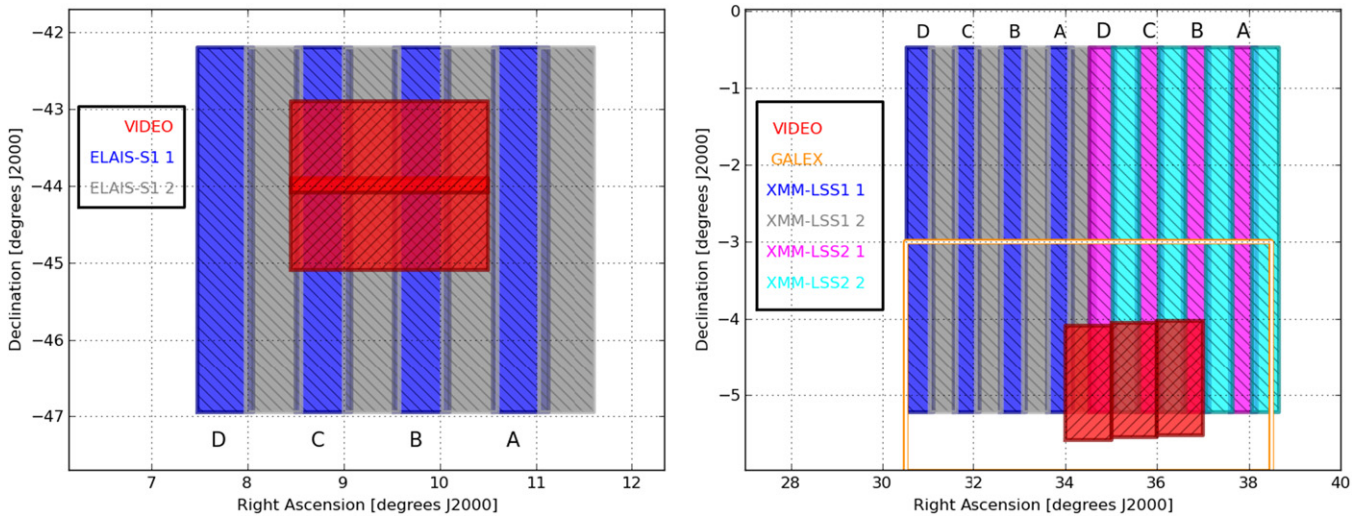
Figure 3. Observing layout for the ELAIS-S1 (right) and the XMM-LSS (left) fields. In blue are shown ELAIS-S1 1 and XMM-LSS1 1 (first tile), in gray ELAIS-S1 2 and XMM-LSS1 2 (second tile), in magenta XMM-LSS2 1 (third tile), and in cyan XMM-LSS2 2 (fourth tile). Each tile is displaced by half a degree from the previous. In red we show the area repeatedly observed by VIDEO, and we flag the position of the four (A, B, C, and D) fingers for the first tile.

Darks are combined to obtain a master dark for each detector and each exposure time. Then we subtract the master dark of the appropriate exposure time from the science images. The pixel-to-pixel variations of the science frames are corrected, - dividing them by the master flats obtained as we describe below. Finally, bad pixels in the science frames are interpolated using the IRAF task FIXPIX, which requires a bad pixel mask as input. We constructed bad pixel masks for each detector. To construct the bad pixel mask, we use the IRAF task CCDMASK, taking as input the ratio between a high-count twilight flat and a low-count twilight flat.

Given the large size of the camera and the large field of view of the telescope, to obtain dome flats using a uniformly illuminated panel was unfeasible. Furthermore, the automatic operation of the telescope complicates a careful acquisition of dome flats. Instead, twilight flats were preferred because they can be easily acquired automatically. Typically twilight flats are taken at the beginning (evening flats) and the end (morning flats) of the observing night. On many occasions flats were not useful because of Moon illumination gradients, a closed dome, or cloudy conditions.

To avoid these problems and to obtain a good pixel-to-pixel variation correction, we selected, from dark-subtracted and trimmed twilight flats, the flats with mean counts above the average obtained over approximately 2 weeks of observations. Then we median combine these twilight flats and normalize them to obtain master flats for each detector. Typically, we combined more than 50 twilight flats per detector.

5. ASTROMETRY

5.1. Astrometric Solution

The frame headers lack basic astrometric information. To solve for this, we have created basic astrometric headers that contain a crude approximation to the true World Coordinate System (WCS) information of the frame. We introduce the estimated header keys (i.e., an estimated WCS) into the image headers using MissFITS.[8] Then we proceed to obtain a first

good astrometric solution using astrometry.net[9] (Lang et al. 2010). This software provides a fast and robust method to calibrate astronomical images and is able to produce a *blind astrometric calibration* of the QUEST frames. The output is an image with WCS information that can be further refined.

The solution produced by astrometry.net is refined using the Software for Calibrating AstroMetry and Photometry (SCAMP; Bertin 2006). SCAMP is a program that computes precise astrometric projection parameters from source lists obtained directly from FITS images. The input lists for SCAMP are in SExtractor binary format ("FITS_LDAC"; Bertin & Arnouts 1996) and must contain the centroid coordinates, centroid errors, astrometric distortion factors, flux measurements, and flux errors. Furthermore, SCAMP creates frame headers ready to be used in an image-stacking process. Both astrometry.net and SCAMP used the reference catalog USNO-B (Monet et al. 2003), which has an astrometric accuracy of $0''2$.

5.2. Assessment of QUEST Astrometry

To test the precision of our astrometric solution, we assessed the internal astrometry by computing the standard deviation of the internal cross-matching of sources. To assess the absolute astrometric precision, we cross-matched our source catalogs with SDSS sources, and then we computed residuals of the cross-matching.
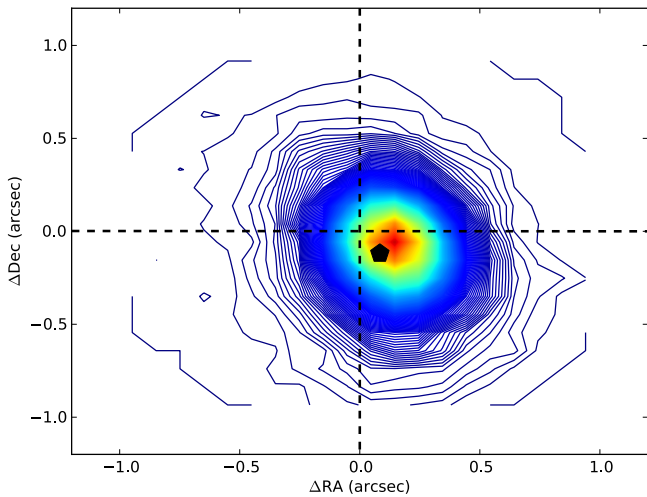
5.2.1. Internal QUEST Astrometric Consistency

To study the astrometric consistency, we defined two samples of point-like sources: the subsample called standard stars and the subsample of variable objects. We used a χ^2_{LC} statistic (where LC stands for light curve, generated as detailed in Section 6.7; see Sesar et al. 2007) to distinguish between standard stars and variable objects, which is defined as follows:

$$\chi^2_{\mathrm{LC}} = \frac{1}{(n-1)} \sum_{i=1}^{n} \frac{(m_i - \bar{m})^2}{\sigma_i^2}, \qquad (1)$$

---

[8] http://astromatic.net/software/missfits

[9] http://astrometry.net/

Figure 4. Astrometric comparison between QUEST and SDSS positions for all point sources in our COSMOS field. The figure shows the contour level lines of the number of objects as a function of ΔR.A. and Δdecl., where ΔR.A. corresponds to $\alpha_{SDSS} - \alpha_{QUEST}$ and Δdecl. to $\delta_{SDSS} - \delta_{QUEST}$. The black dashed lines show the zero offset axis, and the black pentagon marks the position of mean offset.

where n is the number of detections, m_i is the magnitude, $\bar{m}$ is the mean magnitude, and σ_i is the photometric error. The standard-star subsample consists of objects with $n > 10$, a standard deviation in its light curve (σ_{LC}) smaller than the median error observed in the photometry (σ_{median}), $\sigma_{LC} < 0.035$ mag, and $\chi^2_{LC} < 1.5$. The other group, called variables, contains objects with $n > 5$, $\sigma_{LC} > 2 \times \sigma_{median}$, $\sigma_{LC} > 0.05$ mag, and $\chi^2_{LC} > 2.0$. As an example, we obtained roughly 19,800 standard stars in our COSMOS field, of which 18,265 have SDSS counterparts with good photometry. Of the 2790 variable objects in our COSMOS field, roughly 2500 have SDSS counterparts with good photometry.

We computed the mean and the median dispersion in the equatorial (J2000) position of the standard stars and obtained $0''.08$ and $0''.07$, respectively. The standard deviation for this subsample was $0''.04$. For the variable subsample the mean and the median were $0''.15$ and $0''.11$, respectively. The standard deviation for the variables was $0''.10$. The variable subsample has many bright variable stars and relatively faint transients. When the bright variable stars brighten, the PSF of these bright stars is close to saturation, such that the centroid becomes more uncertain. Something similar happens with faint transients where the centroid is more uncertain owing to background fluctuations. In addition, after inspection of the light curves, we found a significant number of non-variable sources classified as variables owing to matching with nearby artifacts, thus leading to an increase in the astrometric dispersion. Overall, our internal astrometric precision is typically $\sim 0''.1$.

5.2.2. QUEST versus SDSS Astrometric Consistency

To assess our overall accuracy, we cross-matched our QUEST subsample catalogs with SDSS stars. For the standard subsample we obtained a mean of $0''.21$ with a standard deviation of $0''.13$, and the median was $0''.18$. In the case of the variable group we obtained a mean of $0''.23$ with a standard deviation of $0''.17$, and a median of $0''.19$. As before, some of

the variable sources may be contaminated by matching with artifacts, thus increasing the dispersion in their positions.

In Figure 4 we show an astrometric comparison between QUEST positions and SDSS positions for all point sources in our COSMOS field. We found mean offsets of $\alpha_{SDSS} - \alpha_{QUEST} = 0''.08$ with a dispersion of $0''.25$, and $\delta_{SDSS} - \delta_{QUEST} = -0''.12$ with a dispersion of $0''.19$. We found that these offsets are variable across the field (see Figure 5) and possibly are related to small systematic differences between SDSS and USNO-B, since both astrometry.net and SCAMP used as a reference catalog USNO-B (Monet et al. 2003), which has an accuracy of $0''.2$. Therefore, the differences in the positions between QUEST and SDSS objects are within the expected astrometric accuracy of the reference catalogs.

6. PHOTOMETRY

6.1. Q-band Photometric System

The QUEST–La Silla survey uses a broad filter covering from 4000 to 7000 Å, called the Q band. This bandpass was designed to avoid the fringing often present in the images taken as part of the Palomar-QUEST survey (Baltay et al. 2007). In Figure 6 we show an estimation of the system effective response of the Q band (solid black line). We computed the Q-band system response profile using the QUEST filter (dashed black line; see Rabinowitz et al. 2012), the mirror reflectivity (dashed gray line), the Cerro Tololo Inter-American Observatory sky transmission at an airmass of 1.3 (dot-dashed gray line), and the quantum efficiency of the camera (dotted gray line; see Baltay et al. 2007). We assume a flat throughput of 90% for the optics of the camera. For comparison we show the filter response curves of SDSS[10] at an airmass of 1.3. It can be observed that the Q-band system response used in QUEST–La Silla is similar to a broad $(g + r)_{SDSS}$ filter. Therefore, we decided to calibrate the Q-band performing differential photometry using reference stars from SDSS-DR7 (Abazajian et al. 2009) in the COSMOS field.

To calibrate our photometry, we created a catalog of Q magnitudes of SDSS point sources with good g and r photometry. To make this catalog, we transformed g and r magnitudes to flux, and then we added these fluxes to obtain an equivalent to the flux in Q. This flux was transformed to Q magnitudes in the AB system.

6.2. PSF Photometry

We carried out PSF photometry in the QUEST frames using custom scripts that run DAOPHOT (Stetson 1987) on each epoch. We decided to compute PSF photometry, since for faint stellar sources and crowded fields PSF photometry is usually better than aperture photometry. However, PSF photometry is more expensive in computing time. Besides, we find that occasionally QUEST frames can yield a bad PSF owing to telescope tracking problems, bad weather, moonlight scattered into the frames, or frames with too many cosmetic problems.

6.3. Aperture Photometry

We also carried out aperture photometry using SExtractor (Bertin & Arnouts 1996). SExtractor is software for

---

[10] http://classic.sdss.org/dr7/instruments/imager/filters/
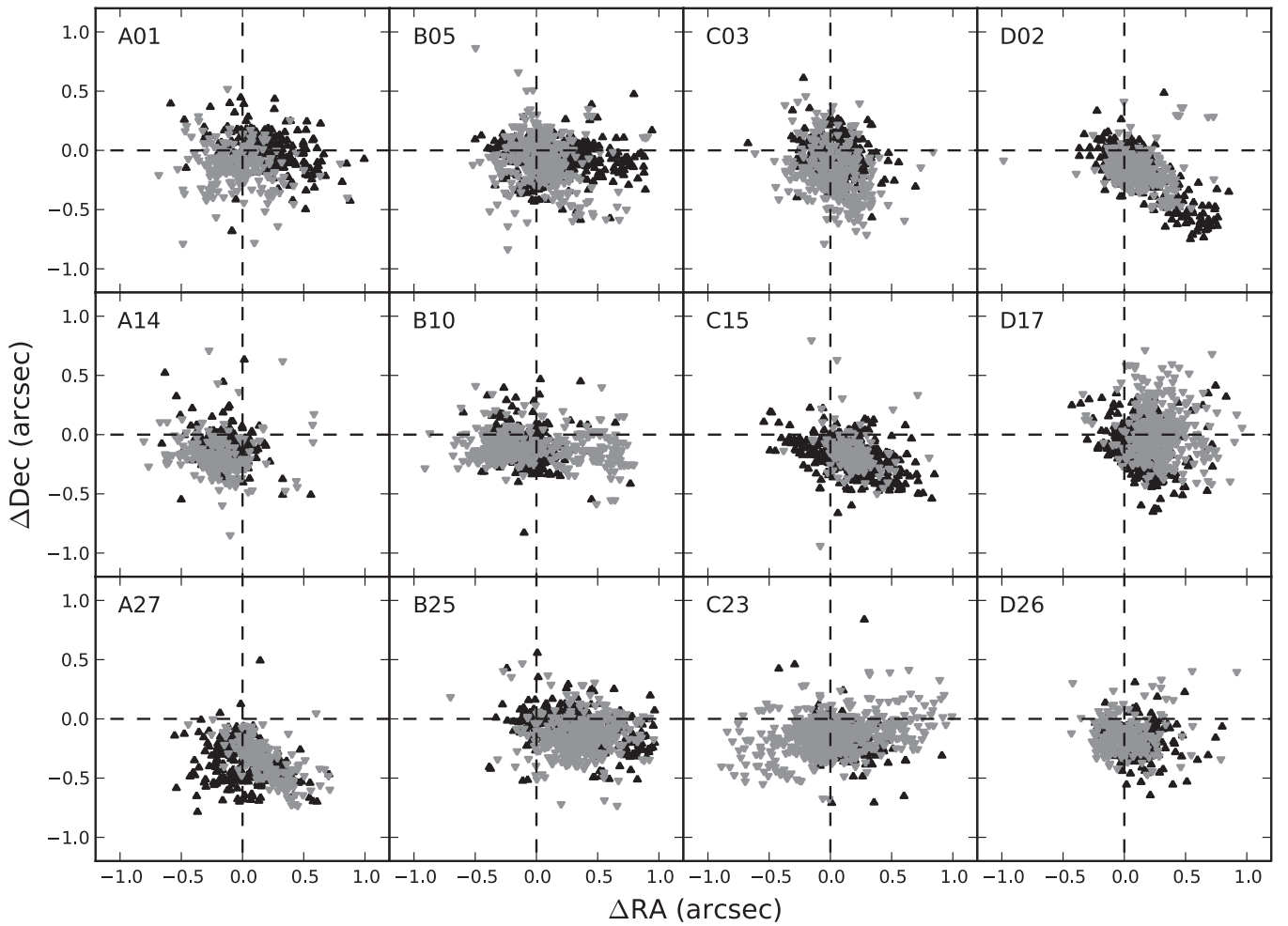
Figure 5. Astrometric comparion between QUEST and SDSS positions for 12 randomly selected detectors. In black we show tile 1 and in gray tile 2. The black dashed lines show the zero offset axis. Overall, the mean offsets are within $0''2$, which is consistent with the astrometric accuracy of USNO-B (Monet et al. 2003).
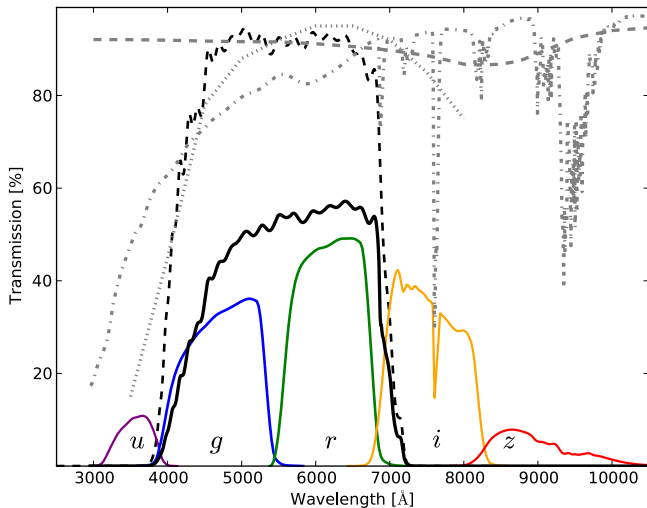
Figure 6. System responses of the SDSS bandpasses (in colors) and the Q band (solid black) at an airmass of 1.3. We computed the Q-band system response profile from the multiplication of the QUEST filter (dashed black; see Rabinowitz et al. 2012), twice the mirror reflectivity (dashed gray), the sky transmission at an airmass of 1.3 (dot-dashed gray), and the camera quantum efficiency (dotted gray; see Baltay et al. 2007). We assume a flat throughput of 90% for the optics of the camera. The Q-band filter covers a spectral region similar to a $(g + r)_{SDSS}$ filter.

computing aperture photometry and other source parameters (e.g., stellarity, source shape, and photometry quality) quickly.

To obtain AGN aperture photometry with minimal contribution from the host galaxy, we determined an optimal aperture of ~ 7 pixels ($\sim 6''18$). This aperture is 2.5–3.0 times wider than the typical seeing of the QUEST–La Silla images, which ranges between $2''0$ and $2''5$, and is relatively insensible to typical seeing variations at the La Silla observatory site.

6.4. Comparison between Aperture Photometry and PSF Photometry

Overall, we found that PSF and aperture photometry agree very well and the differences are within the uncertainties. The mean difference between aperture and PSF photometry is 0.02 mag, with a standard deviation of 0.03 mag. In Figure 7 we compare PSF and aperture photometry for variable stars in the QUEST-COSMOS field.

After a random inspection of the light curves (see Section 6.7) we found that PSF photometry achieves slightly better results for faint point sources, while for the rest of the objects both techniques yield similar results. However, currently our pipeline fails to obtain a PSF solution for a significant number of image frames. Hence, for the AGN variability analysis of Section 7 we use aperture photometry. In
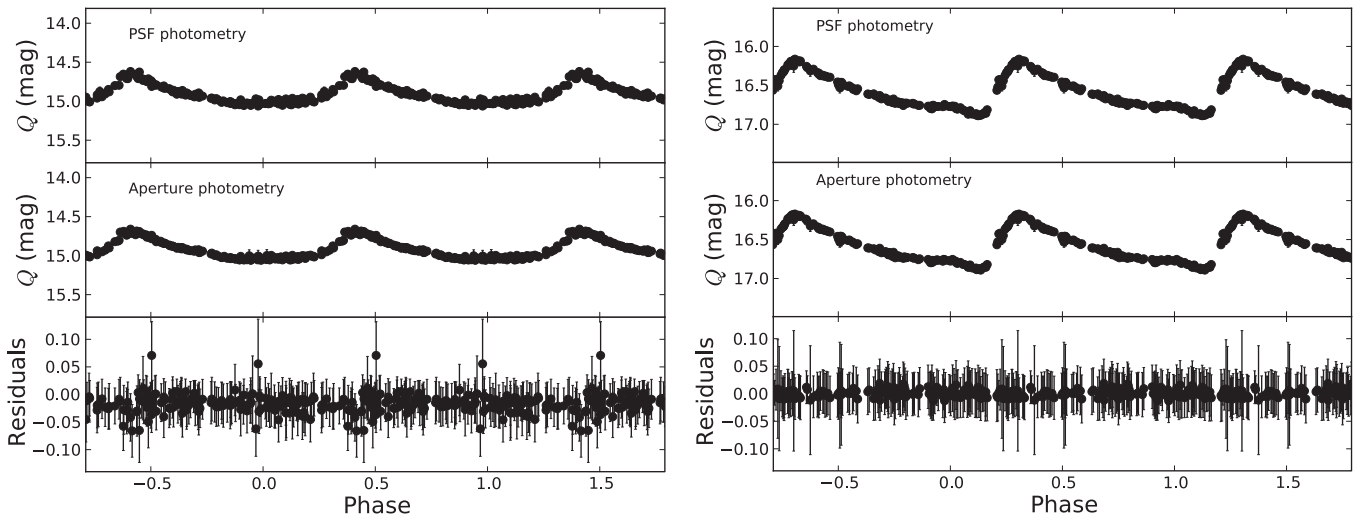
Figure 7. Examples of periodic variable stars in the QUEST-COSMOS field; the left panel star has a period of ~1.44 hr, whereas the right panel object has a period of ~14.59 hr. We present PSF and aperture photometry in the top and middle panels, respectively. In the bottom panel we show the residuals of the difference between PSF and aperture photometry.
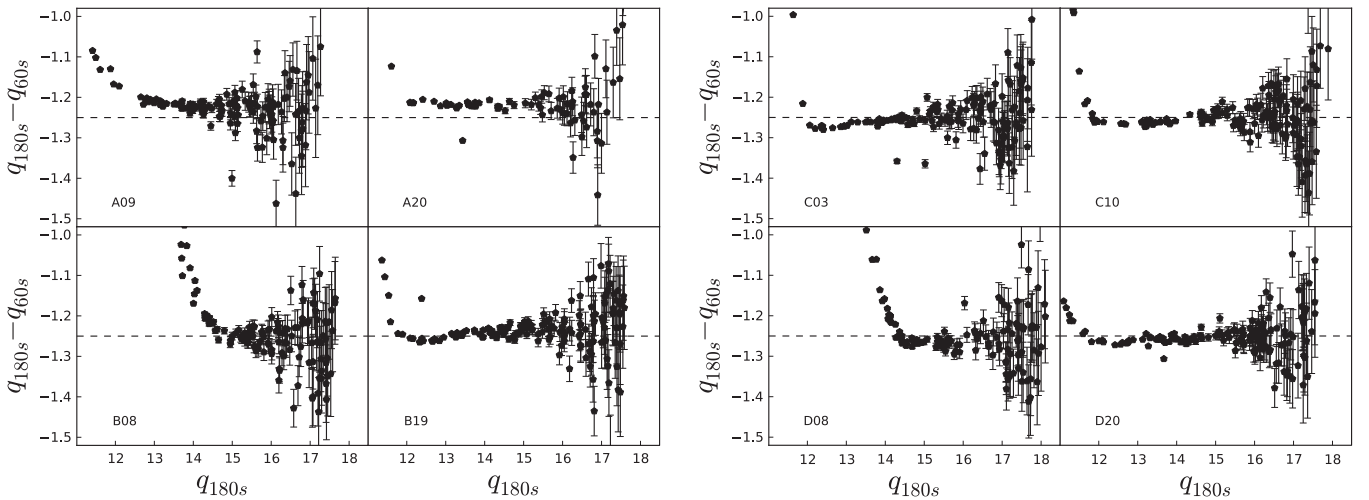
Figure 8. Residuals of the difference between 180 s instrumental magnitudes ($q_{180\,s}$) and 60 s instrumental magnitudes ($q_{60\,s}$) as a function of $q_{180\,s}$ for the detectors of Figure 9. The 180 s and 60 s observations were taken on the same clear night ~5 minutes apart. These examples show how each detector has its own nonlinear behavior. We plot black horizontal dashed lines to guide the eye.

the future we might be able to improve our PSF photometry using ad hoc parameters for each detector.

6.5. Linearity Correction

To ensure that nonlinearity is not a dominant effect in the calibration of our data, we looked at observations of 60 and 180 s taken close in time and on clear nights. In the perfect case where nonlinearities and saturation were unimportant we would expect to see flat residuals for the difference between 180 s instrumental magnitudes ($q_{180\,s}$) and 60 s instrumental magnitudes ($q_{60\,s}$). In Figure 8 we show the residuals of $q_{180\,s} - q_{60\,s}$ as a function of $q_{180\,s}$. In the plots all detectors show a clear upward trend toward the left, corresponding to bright objects. After an inspection of the images, we found that the vast majority of the objects were not saturated, and the most likely explanation for this behavior is nonlinearity of the detector.

Furthermore, the onset of the nonlinearities depends on each detector. For example, in Figure 8 detector A20 has no significant slope, while detector C03 shows a clear positive

slope. A pronounced slope is indicative that nonlinearity is present.

To correct the nonlinearities, we inspected the residuals of the difference between the q instrumental magnitudes and the $(g + r)_{\rm SDSS}$ magnitudes as a function of q. In Figure 9 we show some examples of $q - (g + r)_{\rm SDSS}$ as a function of the instrumental magnitude. For most of the examples a linear fit as a function of q is a significantly better representation of the residuals than a constant zero point. For this reason we decided to use a linear expression of the following form to fit the residuals:

$$q - (g + r)_{\rm SDSS} = \alpha + \beta \times q. \tag{2}$$

To avoid distortions in the fit due to very bright and faint sources, we only used objects in the interval $13.5 < q < 17.5$ (shown in black), and we σ-clipped the fit to eliminate outliers (gray triangles). Figure 9 shows that this model produces good fits to the residuals, even to the data points that were not used to compute the linear model.
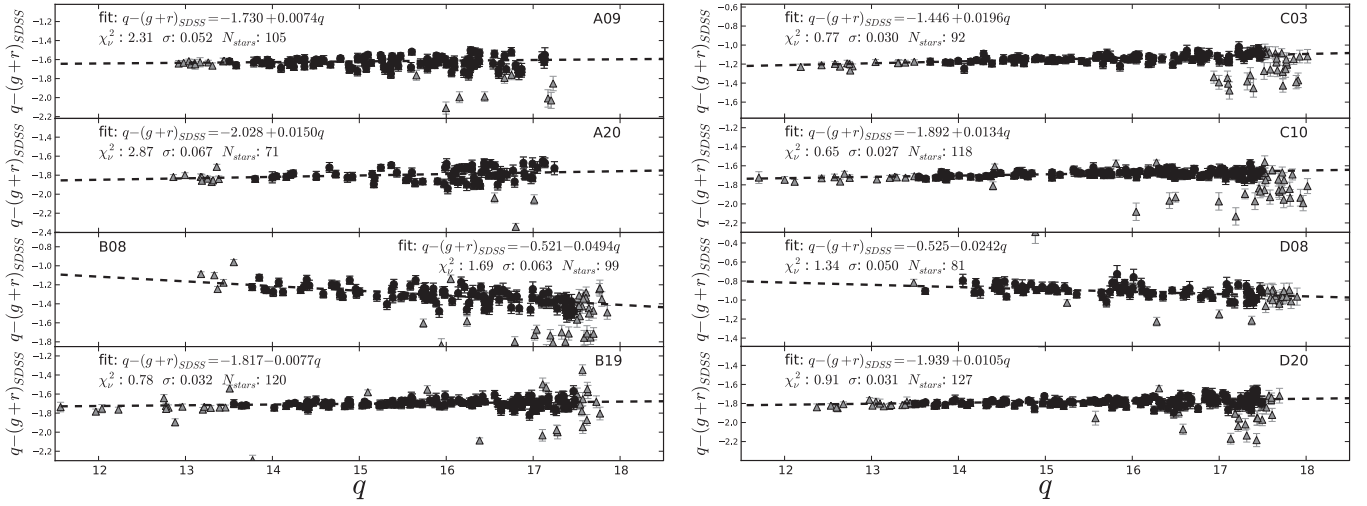
Figure 9. Residuals of the difference between the QUEST instrumental magnitudes (q) and the $(g + r)_{SDSS}$ magnitudes for stars plotted as a function of q. The black points correspond to the data used to compute the photometric zero point as a function of q (dashed black line). Gray triangles are point sources with $q < 17.5$ or $q > 13.5$, or are outliers to the fit, and they were not used to compute the best linear fit. On the top of each panel we give the best-fit parameters and the detector name.
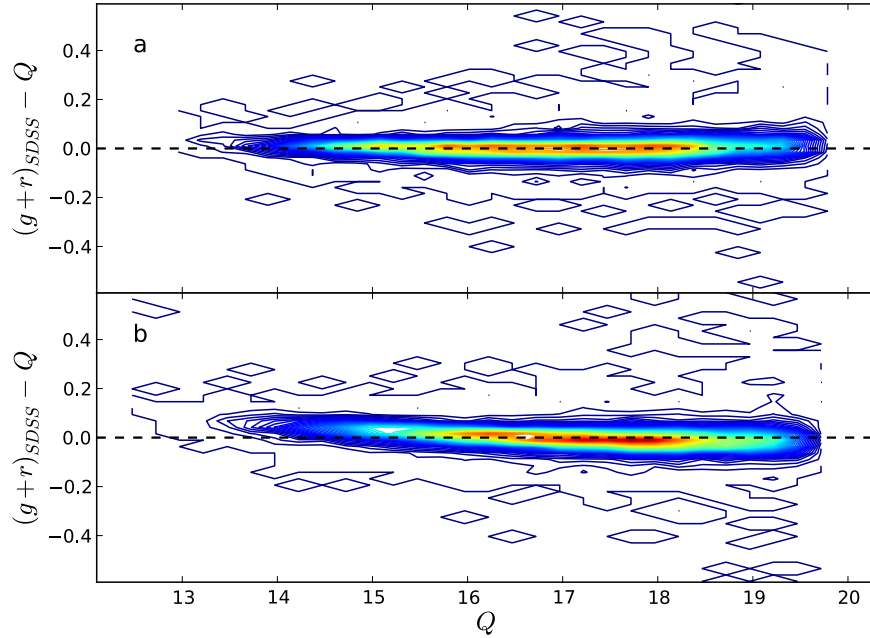
Figure 10. Contour level lines of the number of stars as a function of the residual magnitude, and the Q-band magnitudes for more than 15,000 stars. The residual is the difference between the $(g + r)_{SDSS}$ magnitude and the mean Q-band magnitude of the stars. These stars were flagged as standards based on our 2011 observations. In panel (a) the Q-band calibration was done using our linearity correction technique (see Section 6.5), while in panel (b) the Q-band calibration was done using a constant zero point.

We determine the reduced χ^2 (χ^2_ν), the standard deviation (σ), and the number of stars used to compute the fit. Subsequently, we use these parameters to clean our photometry from bad epochs when constructing the light curves. We discard photometry with $\chi^2_\nu > 10$, $\sigma > 0.1$, or photometry that was obtained with less than 20 stars in the calculation of the zero point (see Section 6.7). The final calibrated Q-band magnitude is computed as

$$Q = q \times (1 - \beta) - \alpha. \qquad (3)$$

In Figure 10 (top panel) we show the residuals of Q minus the $(g + r)_{SDSS}$ magnitude for 18,265 non-variable stars where

the calibration of the Q magnitudes was done following the prescription described above. These stars were classified as standards following the same criteria of Section 5.2.1, namely, $n > 10$, a standard deviation in its light curve smaller than the median error observed in the photometry, a $\sigma_{LC} < 0.035$ mag, and $\chi^2_{LC} < 1.5$. As shown in the top panel of Figure 10, we obtained a good correspondence between $(g + r)_{SDSS}$ and Q magnitudes, with a mean residual of 0.004 ± 0.048 mag.

If instead we had used a constant zero point to calibrate the observations, where we used σ-clipping to clean for outliers, we would have obtained 16,977 standard stars with the
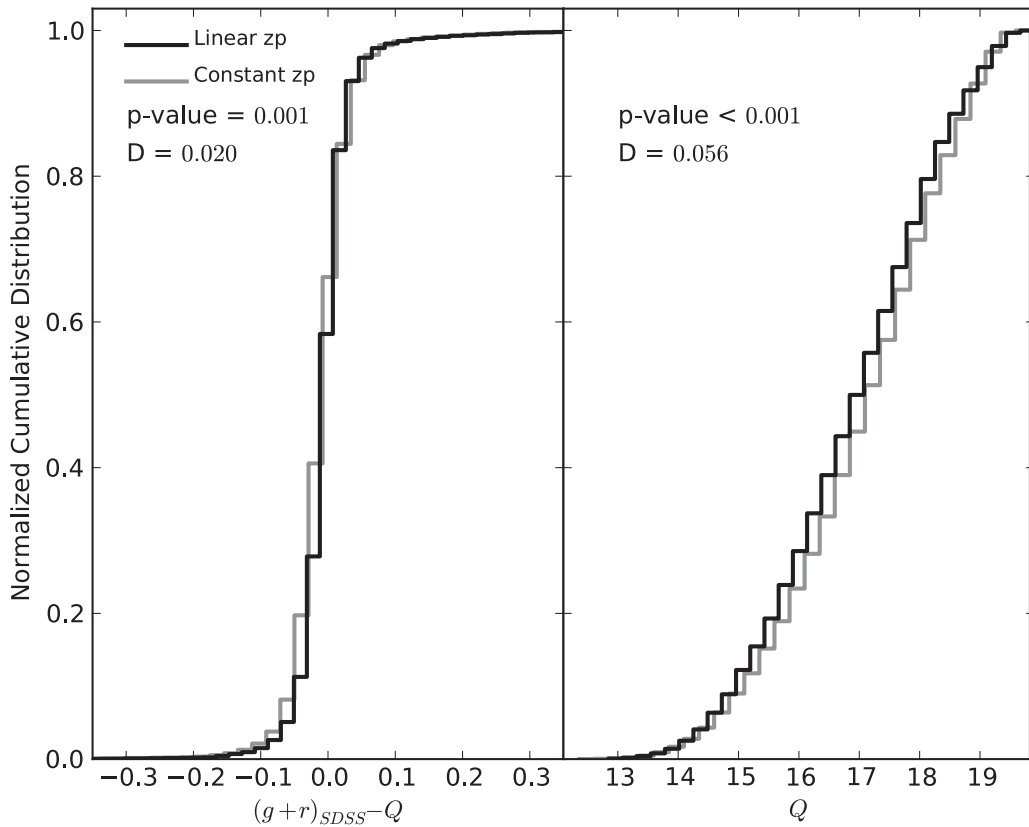
Figure 11. Left panel: normalized cumulative distributions of $Q - (g + r)_{\rm SDSS}$ residuals for non-variable point sources for the case of a constant zero point (gray) and for a linear model calibration (black). Right panel: normalized cumulative distributions of Q magnitude for non-variable point sources for the case of a constant zero point (gray) and for a linear model calibration (black). The *p*-value and the K-S D parameter are indicated on the left of each panel.

$(g + r)_{\rm SDSS} - Q$ residuals shown in the bottom panel of Figure 10. The correspondence between $(g + r)_{\rm SDSS}$ and Q is good, with a mean residual of 0.001 ± 0.052 mag.

Using a linear fit instead of the usual constant zero point reduces the dispersion in the light curves, thus increasing by $\sim 7.5\%$ the number of non-variables or standard stars. Although the means and the standard deviations of the $(g + r)_{\rm SDSS} - Q$ distributions in the case of a linear and constant zero point are consistent with each other, a Kolmogorov–Smirnov (K-S) test yields a *p*-value equal to 0.01. This means that the null hypothesis that both distributions are drawn from the same parent population can be rejected (see Figure 11). Additionally, a K-S test on the Q magnitude distributions yields a *p*-value lower than 0.01, so the null hypothesis that both Q magnitude distributions are drawn from the same parent population can be rejected.

We found that when computing the zero point using a linear model with Equations (2) and (3), the number of non-variables or standard stars increases significantly in the range $15 < Q < 19$ (Figure 11). At the same time, the linear model keeps the mean and the standard deviation of the $(g + r)_{\rm SDSS} - Q$ residual consistent with the case of a constant zero point and reduces the skewness in $(g + r)_{\rm SDSS} - Q$ as a function of Q (see Figure 10).

In summary, we found that the use of a linear model to compute the zero point as a function of q achieves a better calibration of our data, and in the cases where nonlinearity is unimportant (i.e., small β) the photometry remains consistent with the case of a constant zero point.

6.6. Color Term

The agreement between the $(g + r)_{\rm SDSS}$ and the Q band is overall very good. However, we decided to explore the possibility of adding a color term to enhance our calibration.

With an estimation of the Q-band system response at hand, we looked for a relation between the residuals of $Q - (g + r)_{\rm SDSS}$ as a function of the $(g - r)_{\rm SDSS}$ color. We began by multiplying the spectrophotometric standard stars of Hamuy et al. (1992, 1994) with the system response curves of Figure 6. Then we computed $Q - (g + r)_{\rm SDSS}$ and the $(g - r)_{\rm SDSS}$ synthetic colors. The results of the synthetic photometry of Hamuy et al. (1992, 1994) standards are shown as black circles in Figure 12. We modeled the $Q - (g + r)_{\rm SDSS}$ residuals as a function of the $(g - r)_{\rm SDSS}$ colors using a linear relation (dashed line in Figure 12) of the form

$$Q - (g + r)_{\rm SDSS} = -0.359(\pm 0.001)$$
$$- 0.0686(\pm 0.0014) \times (g - r)_{\rm SDSS}.$$
$$(4)$$

To estimate the uncertainty in the parameters of the fit, we randomly selected 20 of the 29 stars, and then we refitted a linear model. We repeated this random selection 50 times, and then we estimated the standard deviation of the adjusted parameters.

We also obtained synthetic photometry of extragalactic sources to investigate whether they follow a relation similar to that of the stars. In Figure 12 we show synthetic photometry obtained from SWIRE templates of AGNs, elliptical galaxies,
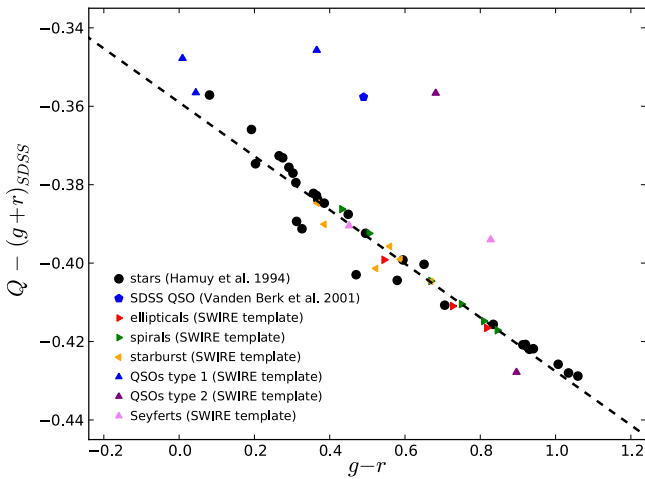
Figure 12. $Q - (g + r)_{SDSS}$ residuals of the synthetic photometry vs. the $(g - r)_{SDSS}$ synthetic colors of the spectrophotometric standard stars of Hamuy et al. (1992, 1994). The black line is the best fit to the stars. Additionally, for comparison we show the $Q - (g - r)_{SDSS}$ residuals of the synthetic photometry vs. $(g - r)_{SDSS}$ synthetic colors of the composite quasar spectra from SDSS (Vanden Berk et al. 2001), in addition to AGNs, galaxies, and starburst galaxy templates from SWIRE (see Polletta et al. 2007).

spiral galaxies, and starburst galaxies (triangles; see Polletta et al. 2007). We additionally show synthetic photometry obtained from an SDSS composite quasar spectrum (blue pentagon; Vanden Berk et al. 2001). Overall, the template of extragalactic sources follows a linear relation similar to that of the stars. The outliers are AGNs, and they depart from the main relation mostly as a result of the presence of strong emission lines.

We used Equation (4) to transform the photometry from the $(g + r)_{SDSS}$ photometric system to the Q band. Then we tested our transformation, performing differential photometry on several nights of 2011. We found that defining the Q band as in Equation (4) does not produce better results than defining the Q band as equivalent to the $(g + r)_{SDSS}$. Indeed, using Equation (4) to compute the Q-band magnitude for the reference stars and then to compute the zero points increases the dispersion in the zero-point calculation and overall produces worse fits.

As a second check on the effects of adding a color term, we performed differential photometry for reference stars on four clear nights of 2011. We then computed the observed color term fitting a straight line to the difference between the instrumental magnitude (q) and the reference $(g + r)_{SDSS}$ magnitudes as a function of the $(g - r)_{SDSS}$ colors. In Figure 13 (left panel) we show the distribution of the observed color - terms obtained. The mean of the distribution is 0.004, the median 0.007, and the standard deviation 0.028. These values are consistent with no color term. However, the large dispersion in the color-term distribution may be explained by a color-term variation between CCDs. Small variations from night to night are also expected.

Formally, the difference between the computed color term using the system responses and the observed color term is 2.59σ. The discrepancy is most likely due to differences between the estimated and the real Q-band system responses. For example, we made a rough assumption of the optics transmission of the camera, and almost certainly there are differences in the quantum efficiency from detector to detector as a function of wavelength.

In conclusion, we find that observations indicate that the color term is close to zero, and therefore the Q band is well described by the $(g + r)_{SDSS}$ system. As a result, we did not apply any color term to our transformation. Nevertheless, there is some uncertainty associated with this assertion. In order to correctly take into account this uncertainty, we added in quadrature a color-term uncertainty equal to $0.03 \times (g - r)_{SDSS}$.

In Figure 13 (right panel) we show the resultant distribution of the observed color terms after adding this color-term uncertainty. The mean of the distribution was 0.00002, the median was 0.002, and the standard deviation obtained was 0.029. Overall, this additional term did not increase the dispersion in the zero-point calculation and produced consistent fits. Therefore, we assume that it is a robust measure of our uncertainty on the filter transmission discrepancies.

6.7. Light-curve Generation

For each epoch and each detector we generated a catalog that contains the equatorial position of the object in degrees (i.e., R. A. and decl.), the calibrated magnitude, the magnitude error, the number of stars used to obtain the photometric zero point, the standard deviation of the zero point, and the reduced χ^2 of the zero-point adjustment (see Section 6.5). Light curves are generated for objects in the matching catalogs of different epochs, but always for the same detector and the same tile. This means that we generate light curves for each tile/detector separately. To match sources, we used a radius of $1''$, which is roughly equivalent to 1 pixel. We avoid contamination from bad nights, which typically have few stars in the zero-point computation and produce a very uncertain photometric zero point. To this effect, we select only those nights that use more than 20 stars to compute the zero points, where $\chi_\nu^2 < 10$, and the standard deviation of the zero-point adjustment is lower than 0.10 mag.

6.8. Systematic Error in the Photometric Zero Point

We assessed systematic differences in our photometry by comparing the magnitudes of stars in the common area of two adjacent tiles offset by $0°.5$. We found that there are 6047 stars detected in two adjacent images of the COSMOS field. The mean difference in their magnitudes is 0.016 ± 0.068 mag, with a median difference of -0.014 mag. In Figure 14 we summarize the mean magnitude differences for each over-lapping area. We investigated the magnitude differences as a function of magnitude dividing the stars into magnitude ranges, and we found that stars in the brighter range have higher systematic differences than fainter stars. Our results are summarized in Table 3.

Based on our results, we quote that our systematic uncertainty is 0.05 mag; this value brings into agreement most of our observed/calibrated photometry in different tiles. We note that this systematic uncertainty is related to variations from detector to detector, and that additional variations are also introduced as a consequence of the use of different stars to compute the zero points. For observations obtained using the same tile/detector it is not necessary to take into account this uncertainty, since we are using the same detector and mostly the same stars to compute the zero point.
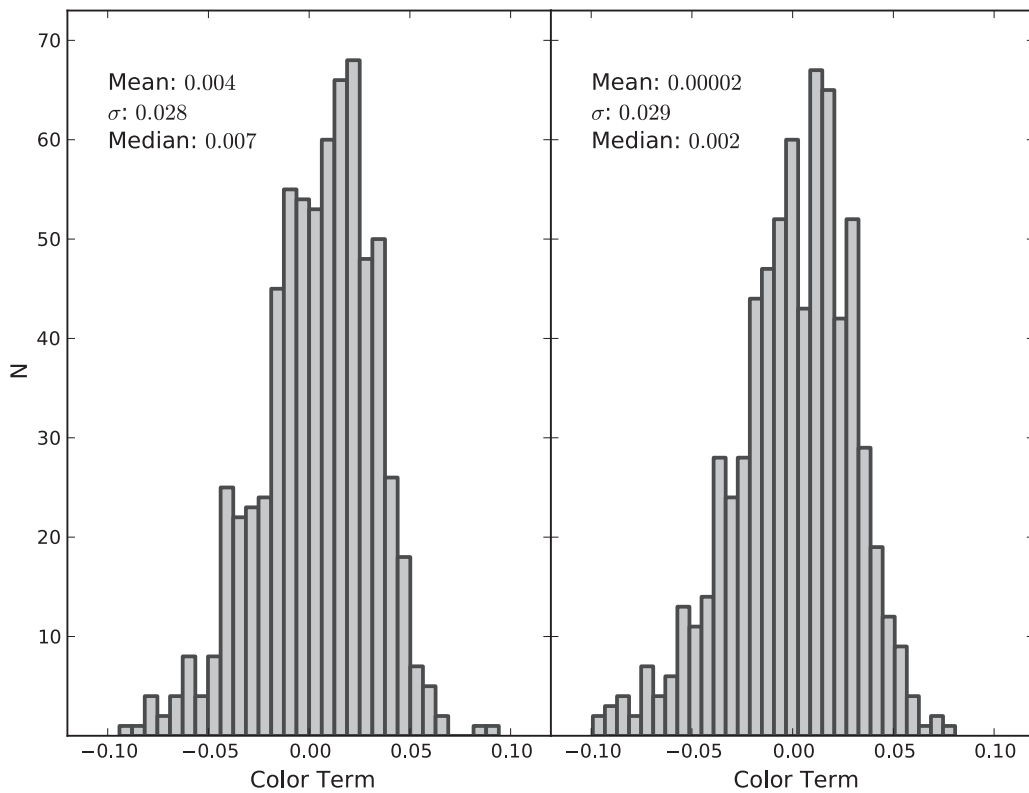
Figure 13. Distribution of the color terms computed from observations of four nights made in 2011. Left panel: color term calculated from a Q-band catalog of stars computed assuming an equivalence between the Q band and the $(g + r)_{\mathrm{SDSS}}$ band (i.e., zero color term) but not taking into account the uncertainty in the color-term correction. Right panel: color term calculated from a Q-band catalog of stars computed assuming an equivalence between the Q band and the $(g + r)_{\mathrm{SDSS}}$ band but taking into account the uncertainty in the color-term correction (see text). The mean, the median, and the standard deviation of the distributions are given in the top left of each panel.
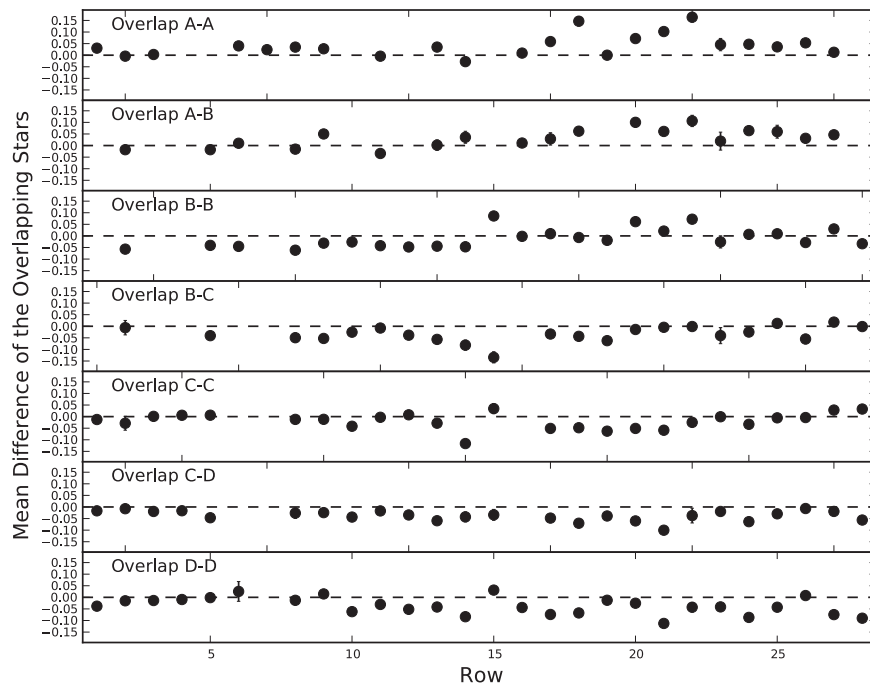
Figure 14. Mean differences for the stars in common for each overlapping area. The corresponding overlapping area is indicated in the top left of each panel.

Table 3
Magnitude Difference of the Overlapping Stars

Range	N_{Stars}	$\langle \Delta Q \rangle$	σ	$\Delta Q_{\mathrm{Median}}$
$Q < 14.0$	40	-0.044	0.065	-0.036
$14.0 < Q < 15.5$	316	-0.020	0.056	-0.016
$15.5 < Q < 17.0$	1501	-0.019	0.068	-0.015
$17.0 < Q < 18.5$	2844	-0.015	0.067	-0.013
$Q > 18.5$	1346	-0.014	0.073	-0.014
$15.5 < Q < 18.5$	4345	-0.016	0.067	-0.014
Total	6047	-0.016	0.068	-0.014

7. OPTICAL VARIABILITY OF XMM-COSMOS X-RAY-SELECTED AGNs

In this section we study the optical variability properties of the XMM-COSMOS X-ray-selected AGNs. To do this, we constructed optical light curves using the 2010–2012 data for 287 QUEST detected sources out of the 1797 X-ray point sources presented in Table 2 of Brusa et al. (2010) (the X-ray catalog hereafter). Most of the objects contained in the X-ray catalog are faint optical sources with a mean r magnitude of $\sim$22.9 and a standard deviation of 1.9 mag in their r magnitude distribution. Overall, we detected $\sim$76% (254 objects) of the sources in the X-ray catalog to a limiting magnitude of $r \sim 21$. The X-ray catalog contains X-ray, optical, infrared, spectroscopic, and photometric redshift information for the XMM-COSMOS sources. To construct this multiwavelength data set, Brusa et al. (2010) cross-correlated X-ray positions with the optical multiband catalog of Capak et al. (2007), the Canada–France–Hawaii Telescope K-band catalog (McCracken et al. 2010), the IRAC catalog (Sanders et al. 2007; Ilbert et al. 2009), and the 24 μm MIPS catalog (Le Floc'h et al. 2009). Additionally, they used accurate C-Chandra (Elvis et al. 2009) positions available for a subset of objects within an area of $\sim$1 deg^2 to control-check the optical/near-IR identifications and to assess the reliability of the proposed identifications.

Good-quality spectroscopic redshifts for the optical counterparts are available from *Magellan*/IMACS and MMT observation campaigns ($\sim$530 objects; Trump et al. 2007, 2009), from the VIMOS/zCOSMOS ($\sim$580 objects; Lilly et al. 2007, 2009), or were already present either in the SDSS catalog ($\sim$100 objects; Kauffmann et al. 2003; Adelman-McCarthy et al. 2006) or in the literature ($\sim$95 objects; Prescott et al. 2006). Using this large spectroscopic data set, Brusa et al. (2010) divided the extragalactic sources with available spectra into three classes, on the basis of a combined X-ray and optical spectroscopic classification.

1. *Broad-line AGN* (*BL AGN*): all objects having at least one broad (FWHM > 2000 km s^{-1}) optical emission line in the available spectrum (421 sources).
2. *Non-broad-line AGN* (*NL AGN*): all objects with unresolved, high-ionization emission lines, exhibiting line ratios indicative of AGN activity; if lines are not detected or the observed spectral range does not allow us to construct line diagnostics, objects with rest-frame hard X-ray luminosity in excess of 2 × 10^{42} erg s^{-1}, typical of AGNs (370 sources).
3. *"Normal" galaxies* (*GALs for short*): all sources with unresolved emission lines consistent with spectra of star-forming galaxies or galaxies showing only absorption
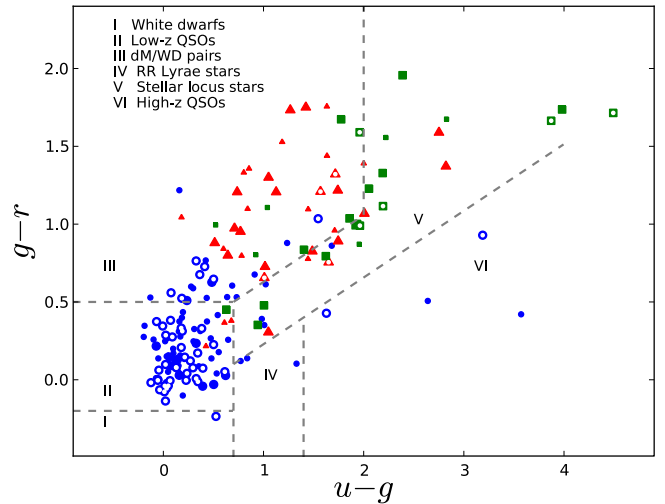
Figure 15. $u - g$ vs. $g - r$ color–color diagram for all the XSMM-COSMOS extragalactic sources detected in the QUEST–La Silla survey. Blue points correspond to BL AGNs, red triangles to NL objects, and green squares to GAL sources. Larger symbols are used to highlight the best sample, and white spots identify variable sources (see Section 7.2). To guide the eye, we show the division used in Sesar et al. (2007) as gray dashed lines, corresponding to regions where different subclasses of variable objects are dominant. The classes are listed in the top left of the figure. The photometry corresponds to model magnitudes obtained from the SDSS-DR7 database, using a cross-matching radius of 0.″3 to match objects. The photometry was corrected using Galactic extinction values given by SDSS, which make use of the extinction maps of Schlegel et al. (1998).

lines, and with rest-frame hard X-ray luminosity lower than 2 × 10^{42} erg s^{-1}, or undetected in the hard band (53 sources).

7.0.1. $u - g$ Color versus $g - r$ Color

In Figure 15 we show the $u - g$ versus $g - r$ color–color diagram for all the XMM-COSMOS extragalactic sources detected in our survey constructed using SDSS-DR7 photometry (Abazajian et al. 2009). In the figure blue circles correspond to BL AGNs, red triangles to NL AGNs, and green squares to GALs. We use larger symbols to highlight the best observed sample defined below in Section 7.2, and a white spot to identify variable sources (see Section 7.2). To guide the reader's eye, we plot the division used in Sesar et al. (2007) as gray dashed lines, which corresponds to regions where different subclasses of variable objects are dominant. For example, in regions II and VI the dominant classes of variable objects are low-z and high-z QSOs, respectively.

The photometry corresponds to model magnitudes obtained from the SDSS-DR7 database (Abazajian et al. 2009), using a cross-matching radius of 0.″3 to match objects. Using this cross-matching radius, we find that 97% of BL AGNs, 88% of NL AGNs, and 83% of GALs have an SDSS counterpart. The photometry was corrected using Galactic extinction values given by SDSS, which make use of the extinction maps of Schlegel et al. (1998).

From the figure it is clear that in the $u - g$ versus $g - r$ color–color space BL AGNs, NL AGNs, and GALs occupy roughly different regions. While BL AGNs tend to be concentrated in region II (low-z QSOs), with a few objects in region VI (high-z QSOs) and a non-negligible fraction of

Table 4
QUEST–La Silla AGN Variability Survey Completeness in the COSMOS Field

Range	n_{det}	n_{det}/n_{tot}	$n_{det}^{bl}/n_{tot}^{bl}$	n_{det}^{bl}/n_{det} (n_{tot}^{bl}/n_{tot})	$n_{det}^{nl}/n_{tot}^{nl}$	n_{det}^{nl}/n_{det} (n_{tot}^{nl}/n_{tot})	$n_{det}^{ga}/n_{tot}^{ga}$	n_{det}^{ga}/n_{det} (n_{tot}^{ga}/n_{tot})
1	2	3	4	5	6	7	8	9
$17 < r < 18$	9	0.75	…	0.00(0.00)	1.00	0.33(0.25)	0.62	0.56(0.67)
$18 < r < 19$	26	0.87	0.80	0.31(0.33)	0.80	0.15(0.17)	0.88	0.27(0.27)
$19 < r < 20$	58	0.74	0.72	0.45(0.46)	0.73	0.19(0.19)	0.75	0.16(0.15)
$20 < r < 21$	107	0.67	0.74	0.62(0.57)	0.59	0.16(0.18)	0.60	0.06(0.06)
$21 < r < 22$	30	0.12	0.20	0.67(0.40)	0.06	0.17(0.32)	0.00	0.00(0.04)
$22 < r < 23$	3	0.01<	0.02	0.67(0.33)	0.01<	0.33(0.33)	0.00	0.00(0.01<)

objects in region III (dM/WD pairs), NL AGNs are concentrated in region III, with some objects in region V (stellar locus stars) and very few objects in region II. On the other hand, GALs are concentrated in region V, with a non-negligible fraction of objects in region III. In particular, GAL objects seems to occupy the color–color region between region III and region V.

As expected, BL AGN colors are dominated by AGN emission, while GAL colors are dominated by stellar emission. On the other hand, the optical colors of NL AGNs are consistent with obscured AGNs with some contribution from the host galaxy stellar emission. Since Brusa et al. (2010) classification is partly based on optical spectra, this confirms that the classification is robust and consistent with the optical colors.

7.1. QUEST–La Silla Variability Survey Completeness and Detection Limit

Of the 287 XMM-COSMOS sources detected by QUEST, 233 sources have a corresponding r-band magnitude in the X-ray catalog. The remaining 44 sources are bright, probably saturated, and therefore not included in the optical multiband catalog. In Table 4 we summarize the detection completeness of our survey as a function of r magnitude ranges for easy comparison with other surveys; we also breakdown our analysis for different classes of extragalactic objects. Table 4 is organized as follows: r magnitude range (Column 1); total number of sources detected in our survey in the corresponding magnitude range (Column 2); number of objects detected in our survey over the total number of XMM-COSMOS objects in the corresponding magnitude range (Column 3); number of BL AGNs detected in our survey over the total number of XMM-COSMOS BL AGNs in the same magnitude range (Column 4); number of BL AGNs detected in our survey over the total number of sources detected in our survey, and in parentheses the number of total XMM-COSMOS BL AGNs over the total number of XMM-COSMOS sources in the magnitude range (Column 5); the number of NL AGNs detected over the XMM-COSMOS NL AGNs in the corresponding magnitude range, and in parentheses the number of XMM-COSMOS NL AGNs over the total number of XMM-COSMOS sources in the range (Column 7); the number of GALs detected over the total number of XMM-COSMOS GALs in the range (Column 8); the number of GALs detected over the total number of sources detected in our survey, and in parentheses the number of total XMM-COSMOS GALs over the total number of XMM-COSMOS sources in the range (Column 9).

The survey is roughly 75% complete in the magnitude range between $r \simeq 17$ mag and $r \simeq 20$ mag and slightly less complete (67%) up to $r \simeq 21$ mag. In the range between $r \simeq 21$ and $r \simeq 22$ mag the survey declines to 12% completeness, and the survey drops to less than 1% completeness at fainter magnitudes. If we break down the detection completeness fraction for different object classes ($n_{det}^{class}/n_{tot}^{class}$; see Table 4), we find that the detection completeness fraction, for all classes of objects, is consistent with roughly 75% up to $r \simeq 20$ mag. In the r magnitude range between 20 and 21 mag the detection fraction of BL AGNs is 74%, while the detection fraction of NL AGNs and GALs is 60%. At fainter magnitudes the detection fraction of BL AGNs is significantly higher than that of NL AGNs and GALs. This could be due to strong UV rest-frame emission lines (Lyα, Si IV, C IV, and C III) entering the blue side of the Q band for sources at z > 2.0. When we break down the number of objects detected of a certain class over the total number of objects detected in a magnitude range (n_{det}^{class}/n_{det}; see Table 4), they are in very good agreement with the number of XMM-COSMOS objects of the same class over the total number of XMM-COSMOS objects in the sample (n_{tot}^{class}/n_{tot}; see Table 4) in the magnitude range up to $r \simeq 21$.

The analysis of the detection fractions indicates that we are detecting a large fraction of objects up to $r \simeq 21$. This is in agreement with the limiting magnitude expected based on the exposure time used; for an exposure time of 60 s the expected limiting magnitude is $Q \sim 19.5$, which is equivalent to an r magnitude in the range between 20 and 21 mag. Similarly, for an exposure time of 180 s the expected limiting magnitude is $Q \sim 20.5$, equivalent to an r magnitude in the range between 21 and 22 mag. During 2011 and 2012, most of our observations were performed using exposure times of 60 s, where the completeness below $r \sim 21$ mag is low. Currently (2013–2014), we are performing our observations using exposure times of 180 s, which will increase our completeness at fainter magnitudes.

To illustrate our detection limit as a function of redshift, in Figure 16 we show the Q-band absolute magnitude of the extragalactic XMM-COSMOS objects as a function of redshift. The Q-band absolute magnitudes are not K-corrected or corrected by dust extinction. As can be seen, we are detecting objects up to redshift ~3. In total we detect 29 GALs all below redshift 0.4, 42 NL AGNs all below redshift 1.0, and 123 BL AGNs. In Figure 16 we additionally show the detection limit for an object with $Q = 19.5$ mag (solid line) and the detection limit for an object with $Q = 20.5$ mag (dashed line).

7.2. Variability of the XMM-COSMOS Objects

To study the variability of the XMM-COSMOS extragalactic sources, we defined a flux-limited sample ($Q < 19.5$), where
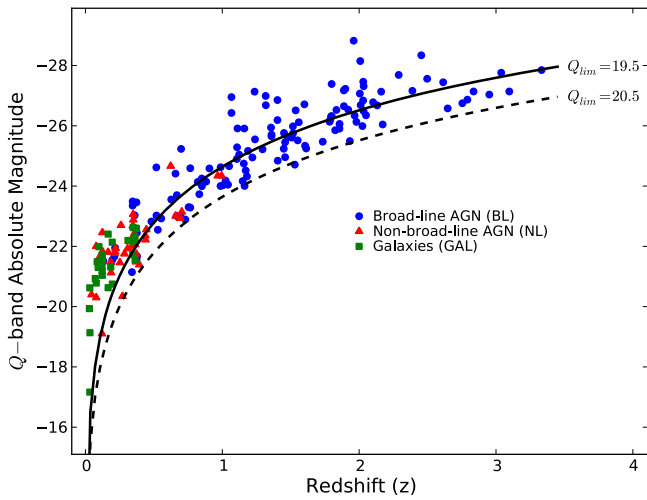
Figure 16. Q-band absolute magnitudes for XMM-COSMOS sources detected as part of our survey. Absolute magnitudes are not K-corrected or corrected by dust extinction. Blue points correspond to broad-line AGNs, red triangles correspond to objects classified as non-broad-line AGNs, and green squares are classified as "normal" galaxies or starburst galaxies. The solid line is the detection limit for an object with $Q = 19.5$ mag, and the dashed line is the detection limit for an object with $Q = 20.5$ mag.

the time lapse between the first and the last observations was more than 600 days. We call this the *best-observed* sample. The time span ensures that the light curves have a significant number of observations. Additionally, the time span longer than 600 days ensures that we will be able to study long-term variability as this corresponds to rest-frame timescales of at least a few months for objects at $z > 0.6$, and of $\gtrsim 1$ year for objects at $z < 0.6$. Our sample of best-observed light curves consists of 55 BL AGNs, 24 NL AGNs, and 23 GALs.

To classify an object as variable or non-variable, we used the variability index V (McLaughlin et al. 1996; Paolillo et al. 2004; Lanzuisi et al. 2014), defined as $V = -\log(1 - P(\chi^2))$, where $P(\chi^2)$ is the the probability that a χ^2 lower than or equal to the observed value could occur by chance for an intrinsically non-variable source. We also defined $P_{var} = 1 - P(\chi^2)$ as the probability of an object being variable. Following Lanzuisi et al. (2014), we defined $V = 1.3$ as our threshold to define a variable object, since an object with $V > 1.3$ has more than 95% probability to be variable ($P_{var} > 0.95$). Based on the V index, we find that 44 (80% ± 5%) of our best-observed BL AGNs are variable, 5 (21% ± 8%) of our best-observed NL AGNs are variable, and 5 (22% ± 9%) of our best-observed GALs are variable. Since the division between variable and non-variable objects is somewhat arbitrary, we assumed a binomial distribution in the classification to estimate the errors. Therefore, based on the binomial distribution three BL AGNs, two NL AGNs, and two GALs may be classified as variable sources by chance.

As a measure of the variability amplitude, we used the excess variance, defined as $\sigma_{rms}^2 = \sigma_{LC}^2 - \sigma_{median}^2$, where σ_{LC} is the standard deviation of the light curve and σ_{median} is the median error of the light curve. In the case where $\sigma_{LC}^2 < \sigma_{median}^2$ we used the median error as an upper limit on the excess variance. In Table 5 we present the distribution of σ_{rms} for our sample of best-observed objects divided into three bins ($\sigma_{rms} < 0.05$, $0.05 < \sigma_{rms} < 0.10$, and $\sigma_{rms} > 0.10$). We found that BL objects tend to have larger variability amplitude, with 77% of the objects showing $\sigma_{rms} > 0.05$ and 23% of the objects

Table 5
Excess Variance Distribution

Range	BL	NL	GAL
$\sigma_{rms} < 0.05$	0.23 (0.20)	0.67 (0.42)	0.67 (0.56)
$0.05 < \sigma_{rms} < 0.10$	0.54 (0.56)	0.17 (0.50)	0.33 (0.35)
$\sigma_{rms} > 0.10$	0.23 (0.24)	0.17 (0.08)	0.00 (0.09)

Note. Fraction of BL, NL, and GAL objects in a given range of σ_{rms} for the best-observed sample. In parentheses we give the fraction of objects in a given range, but now including upper limits.
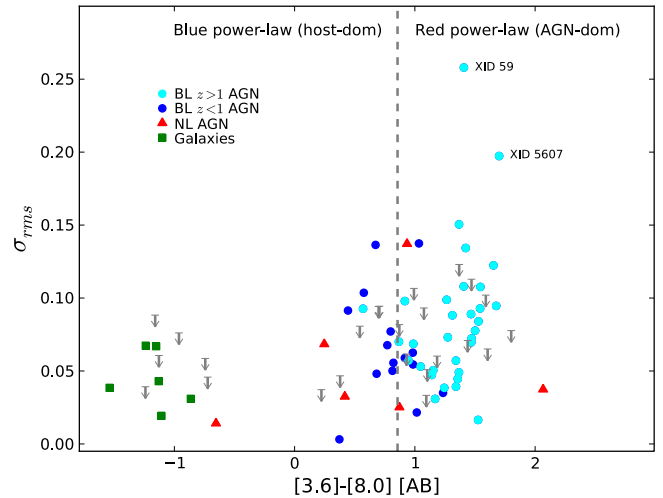
Figure 17. σ_{rms} vs. [3.6]–[8.0] color for the sample of best-observed XMM-COSMOS objects. In the figure cyan cirlces are BL AGNs with $z > 1$, BL AGNs with $z < 1$ are shown as blue circles, red triangles correspond to NL AGNs, and green squares are GALs. The gray dashed line corresponds to the division between AGN-dominated and host-dominated sources of Brusa et al. (2010), and upper limits are shown as gray downward-pointing arrows for BL and NL AGNs, and not shown for GALs for clarity.

with $\sigma_{rms} > 0.10$. On the other hand, 33% of the NL AGNs and GALs have $\sigma_{rms} > 0.05$. Of these, one NL AGN (17%) has $\sigma_{rms} > 0.10$, while all GALs have σ_{rms} below this value. When we include upper limits to the distributions, the tendency remains the same, with 80% of BL AGNs, 58% of NL AGNs, and 44% of GALs having $\sigma_{rms} > 0.05$.

7.2.1. Excess Variance versus [3.6]–[8.0] Color

The mid-IR colors have been proposed as a selection method to identify AGNs (see Lacy et al. 2004; Stern et al. 2005; Kozłowski & Kochanek 2009; Assef et al. 2013, and references therein). The method relies on the fact that the mid-IR emissions of normal galaxies and AGNs have different SEDs. The composite spectra of the stellar population of normal galaxies produce an SED that peaks at approximately 1.6 μm, while AGNs have a roughly power-law SED owing to hot dust emission, which reprocesses the UV/optical emission of the accretion disk, peaking somewhere around 10 μm (Mor & Netzer 2012; Lira et al. 2013). Following this idea, Brusa et al. (2010) showed that the IRAC broadband [3.6]–[8.0] mid-IR color can be used to disentangle objects with infrared-rising SED (red power-law), e.g., AGNs, and sources with an inverted SED (blue power law), e.g., normal galaxies at low z. They used this method to select a sample of highly obscured luminous AGN candidates.

In Figure 17 we explore a tentative relation between the σ_{rms} and the [3.6]–[8.0] mid-IR color for our sample of best-observed BL AGNs, NL AGNs, and GALs. In the figure we show BL AGNs with $z > 1$ using cyan circles, BL AGNs with $z < 1$ using blue circles, NL AGNs with red triangles, and GALs with green squares. The gray dashed line corresponds to the division between AGN-dominated and host-dominated sources of Brusa et al. (2010) ([3.6]−[8.0] = 0.856), and upper limits are shown as gray downward-pointing arrows for BL and NL AGNs, and not shown for GALs for clarity.

As can be seen in Figure 17, BL AGNs show on average large σ_{rms}. Among them there is an apparent trend, although with large scatter, where AGNs with higher σ_{rms} tend to have redder [3.6]–[8.0] colors. This trend is largely driven by BL AGNs, particularly those at $z > 1$ (cyan circles), where the expected contribution from the host galaxy to the Q band is very low. Among the BL AGNs with $z > 1$ the trend seems not to be related to redshift or luminosity. Finally, the BL AGNs with $z < 1$ have bluer colors than the overall BL AGN sample, which implies a higher contribution of host galaxy light to the photometry.

A plausible interpretation for the trend shown in Figure 17 is that AGN variability is diluted by host galaxy light in objects with bluer mid-IR colors (i.e., more host dominated). This will be explored by our collaboration in the future using a larger sample obtained from photometry of stacked images and with light curves with a longer time span.

7.2.2. Structure Function

The structure function is a simple tool to quantify the variability of a source as a function of the time lapse between observations (τ) when a significant number of observations are available. To study the variabilty behavior of our sample as a function of time, we calculated the structure function as

$$\mathrm{SF}(\tau) = \sqrt{\frac{1}{N} \sum_{i=1}^{N} \left[m(t_i) - m(t_i + \tau) \right]^2}, \quad (5)$$

where $m(t_i)$ is the magnitude at time t_i, $m(t_i + \tau)$ is the magnitude at time $t_i + \tau$ in the rest frame, and N is the number of observations in the time span bin. To compute the structure function, we average values in equal size bins in logarithmic space. The bins are "centered" in 2^i days, where the bin interval is $[2^{i-\frac{1}{2}}, 2^{i+\frac{1}{2}}]$ with $i = 0, 1, 2, 3, \ldots$

To take into account the errors in the measurements, we generated a random number drawn from a Gaussian distribution with mean and standard deviation equal to the measurement value and its uncertainty, respectively. Then, we computed the structure function using this mock data set and "normalized" it, removing in quadrature the contribution produced by the signal variance estimated as the median value of the uncertainties in the measurements (σ_{median}).

As is shown in Schmidt et al. (2010) and Palanque-Delabrouille et al. (2011), the structure function of a QSO is well described by a power law, where τ is measured in years, as

$$\mathrm{SF}_{norm}(\tau) = A\tau^\gamma. \quad (6)$$

In Figure 19 we show the power-law exponent (γ) and amplitude (A) that resulted from the power-law fit to our sample. Note that $A = \mathrm{SF}(\tau = 1)$. All the objects classified as variables based on the V parameter are marked with a white

spot on Figure 19. It is clear from the figure that the variability of BL AGNs is on average described by larger A and γ values compared to NL AGNs and GALs. The latter objects tend to be clustered close to $\gamma \simeq 0.05$ and $A \simeq 0.05$ in the γ–A plane. Based on this, we defined the region $\gamma > 0.025$ and $A > 0.1$ in which the observed variability is consistent with being powered by the accretion disk of a supermassive black hole. Therefore, NL AGNs and GALs lying in this region are suspected to show variability consistent with an AGN.

In Figure 18 we investigate the connection between the observed variability in NL AGNs and GALs and the variability powered by the accretion disk of a supermassive black hole represented by BL AGNs. We compare ensemble structure functions of BL AGNs shown in blue, NL AGNs shown in red, and GALs shown in green when we apply different selection criteria to define the sample used to compute the ensemble structure functions. In panel (a) we show the ensemble structure functions when we consider all objects in the best-observed sample; in panel (b) we show the ensemble structure functions when we consider only variable objects ($V > 1.3$); in panel (c) we show the ensemble structure functions when we consider objects located in the BL-AGN-dominated region defined in Figure 19 ($\gamma > 0.025$ and $A > 0.1$); finally, in panel (d) we show the structure functions when we consider objects that are located in the BL-AGN-dominated region (see Figure 19) and are classified as variables according to the V parameter.

In panel (a) it can be seen that when we consider all objects in the best-observed sample, the ensemble structure functions of the NL AGNs and GALs are nearly flat and very different from the AGN-powered variability of BL AGNs that are characterized by an increase of the amplitude of the ensemble structure function as a function of τ. On the other hand, clear variability signatures begin to appear in the ensemble structure functions of NL AGNs and GALs when we consider variable objects (panel (b)) or objects located in the BL-AGN-dominated region in the γ–A plane (panel (c)). However, only when we restrict our selection criteria to variable objects ($V > 1.3$) located in the BL-AGN-dominated region ($\gamma > 0.025$ and $A > 0.1$) do we obtain ensemble structure functions for both NL AGNs and GALs showing variability as a function of τ, consistent with being powered by an AGN (i.e., similar to BL AGNs; see panel (d)). Our sample of variable objects with structure function parameters consistent with AGN-powered variability corresponds to 74.5% (41) of BL AGNs, 12.4% (3) of NL AGNs, and 8.7% (2) of GALs. This implies that 3/5 and 2/5 of the variable NL AGNs and GAL sources selected based on the V index are now securely classified as variable AGNs. This is also consistent with the estimates of false positives derived using the binomial distribution.

7.2.3. Distribution of the [3.6] − [8.0] Color

In the right panel of Figure 20 we show the overall distribution (step-line histogram) of BL AGNs (top panel), NL AGNs (middle panel), and GALs (bottom panel) as a function of the [3.6]–[8.0] color. The distributions of variable sources with $\gamma > 0.025$ and $A > 0.1$ (i.e., SF(τ) similar to BL AGNs) are shown in the panels as shaded histograms. The gray dashed line corresponds to the division between AGN-dominated and host-dominated sources of Brusa et al. (2010).

As expected, all BL AGNs show red colors, with the majority of them consistent with being dominated by the emission from hot dust. Variable BL AGNs do not show any
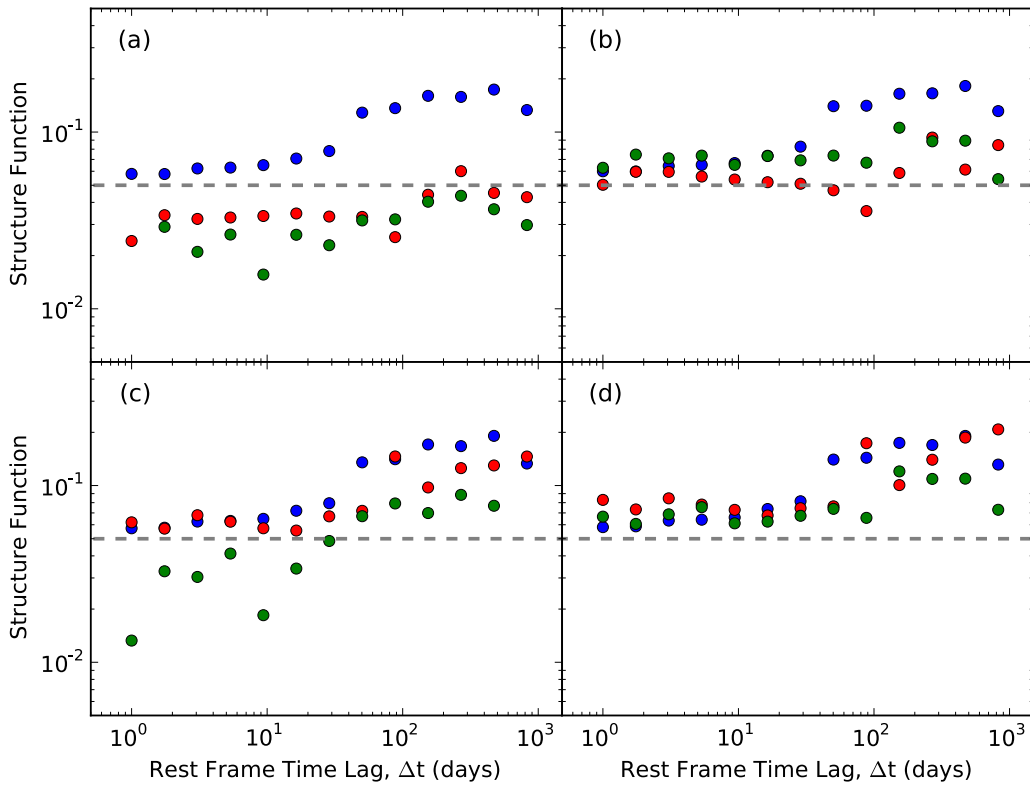
Figure 18. Ensemble structure functions for BL AGNs (blue), NL AGNs (red), and GALs (green) for different subsamples. The dashed gray line corresponds to the 0.05 mag limit value from which any variability signal should dominate over significant noise on the QUEST data. (a) Structure functions for the best-observed sample of BL AGNs ($n = 55$), NL AGNs ($n = 24$), and GALs ($n = 23$). (b) Structure functions for the objects of the best-observed sample classified as variables according to $V > 1.3$, namely, 44 BL AGNs, 5 NL AGNs, and 5 GALs. (c) Structure functions for the objects of the best-observed sample located within the parameter space region of Figure 19 dominated by BL AGNs ($A > 0.1$ and $\gamma > 0.025$), namely, 48 BL AGNs, 7 NL AGNs, and 7 GALs. (d) Structure functions for the objects of the best-observed sample located within the parameter space region of Figure 19 dominated by BL AGNs and classified as variables; 41 BL AGNs, 3 NL AGNs, and 2 GALs.

trend with the [3.6]–[8.0] color. The [3.6]–[8.0] color distribution of NL AGNs shows a large spread. There is a group of NL AGNs with very blue colors and a second group with redder colors peaking on the blue side of the BL AGN distribution and lying close to the division between AGN-dominated and host-dominated sources of Brusa et al. (2010). It is important to mention that, although the NL AGN sample is small, among the objects located on the blue side of the BL AGN color distribution we find the ones with the larger excess variance (see Figure 17). The GALs shows a large spread in the [3.6]–[8.0] color distribution. However, all variable sources have very blue colors and are consistent with being host-dominated objects.

7.2.4. Variability versus HR

The HR can be a measure of the X-ray obscuration suffered by an AGN, and it is defined as HR = (H − S)/(H + S), where S and H are the count rates in the soft (0.5−2.0 keV) and hard bands (2.0−10 keV). High hydrogen column densities (N_H) block soft X-rays; hence, the effect of increasing column densities is that the X-ray spectrum becomes harder. Many studies use an N_H value of 10^{22} cm^{-2} to distinguish between obscured and unobscured AGNs; Mainieri et al. (2007) showed that 90% of the sources with column densities larger than 10^{22} cm^{-2} have HR > −0.3. On the other hand, Hasinger (2008) found that using an HR value of −0.2 as a threshold can distinguish between obscured and unobscured AGNs. We will explore the relation between variability and HR using the latter

value, also used by Brusa et al. (2010), as a threshold. Note that the flux limit in the soft band is ∼6 times fainter than in the hard band (Brusa et al. 2010), and that objects detected only in the soft or hard X-ray band have values of HR = −1 and HR = 1, respectively. While most of our GAL objects have HR = −1, which stems from the Brusa et al. (2010) criteria to classify X-ray sources in the GAL class (see beginning of Section 7), the Hasinger (2008) sample of galaxies shows typical values of −0.2 < HR < 0.5 (see his Figure 2). This can be explained by the fact that Hasinger (2008) used 2–10 keV detected samples only.

In the left panel of Figure 20 we show the overall distribution (step-line histogram) of BL AGNs (top panel), NL AGNs (middle panel), and GALs (bottom panel) as a function of HR. The distributions of variable sources with $\gamma > 0.025$ and $A > 0.1$ (i.e., SF(τ) similar to BL AGNs) are shown as shaded histograms. The gray dashed line corresponds to HR = −0.2, the division between unobscured (low N_H) and obscured (high N_H) AGNs. Using this threshold, we find that 96% ± 3% (53 ± 1) of the BL AGNs are unobscured, while 54% ± 10% (13 ± 2) of the NL AGNs are unobscured according to this definition. Of the GALs, 91% ± 6% (21 ± 1) are characterized by HR < −0.2 and therefore show a soft X-ray spectrum (notice that Hasinger 2008 decided to classify objects without a spectroscopic AGN classification but with HR < −0.2 as a BL AGN, and therefore, under this scheme, the great majority of our GAL objects should be reclassified as AGN).
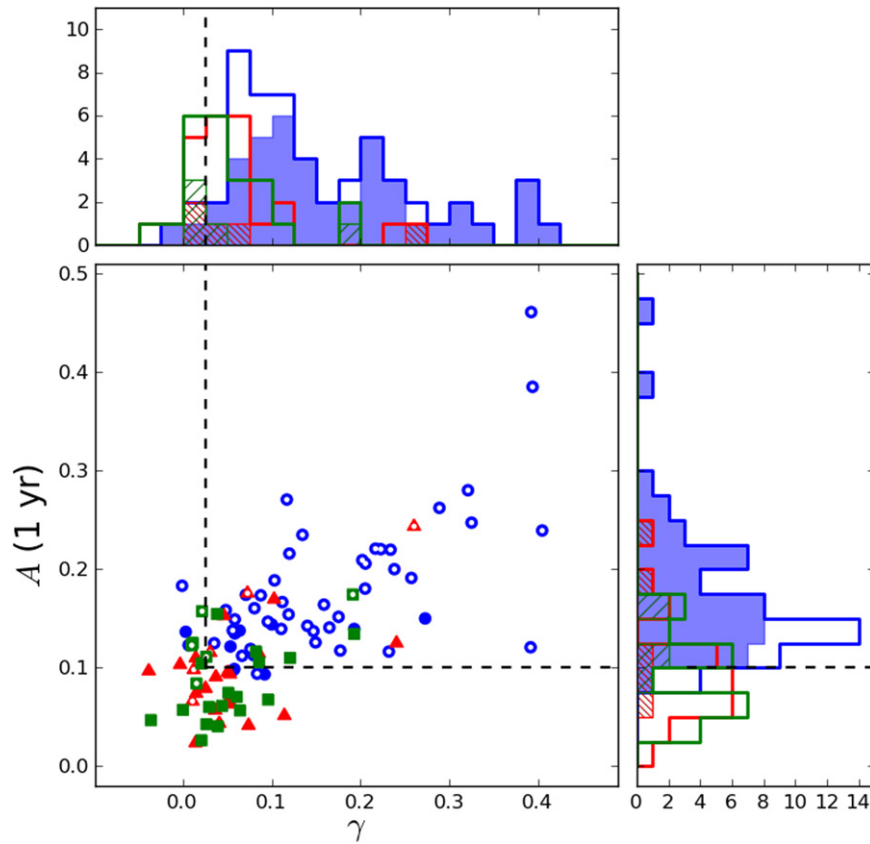
Figure 19. Amplitude (A) and power-law exponent (γ) obtained from fitting a power law to the structure function to the best-observed sample of BL AGNs (blue), NL AGNs (red), and GALs (green). We mark with a white spot the objects classified as variables based on the V parameter (see Section 7.2). In the top panel we show the distribution of the γ for BL AGNs (blue line), NL AGNs (red line), and GALs (green line). In the top panel the blue shaded distribution corresponds to variable BL AGNs, while the red and green hatched distributions correspond to variable NL AGNs and GALs, respectively. Similarly, in the right panel we show the distributions of the amplitude (A). The black dashed line demarcates the region in the A–γ parameter space dominated by BL AGNs (namely, $A > 0.1$ and $\gamma > 0.025$), and therefore the region where the observed variability can be considered as being powered by the accretion disk of a supermassive black hole.

Following our definition of variability consistent with being produced by the accretion disk of a supermassive black hole ($V > 1.3$, $\gamma > 0.025$, and $A > 0.1$), we find that $98\% \pm 2\%$ (43 ± 1) of the BL AGNs that meet these criteria are unobscured, 100% (3) of the NL AGNs that meet these criteria are obscured, and, assuming that the X-ray emission of the GALs that meet these criteria is produced by low-luminosity AGNs, 100% (2) of them are unobscured. As was expected beforehand, the majority of the variable BL AGNs are unobscured. However, it is interesting that, although in the NL AGNs there is a large spread in the HRs and 54% of them are unobscured in the best-observed sample, all the variable NL AGNs are obscured (see Figure 20). This result is also confirmed by the fact that the variable NL AGNs with the larger variability amplitude ($\sigma_{rms} > 0.05$ mag) are among the obscured objects. The most likely interpretation is that a fraction of the accretion disk emission is leaking through the obscuring material.

7.3. The XMM-COSMOS Variable Objects

In Figure 21 we show eight light curves of the most optically variable sources among the XMM-COSMOS objects whose observed variability is consistent with being produced by an AGN, including the three NL AGNs and the two GALs that are variables, and their structure function parameters are consistent with variability produced by an accretion disk as in the case of BL AGNs. In the top right of each panel the XMM-COSMOS

identifier number for each object is shown, while the properties of the objects are summarized in Table 6. All BL AGNs show clear variability with large amplitudes ($\sigma_{rms} > 0.05$ mag). The NL AGNs show mid-IR colors close to the division between AGN- and host-dominated objects and all have HR values consistent with gas obscuration. A likely interpretation for these objects is disk emission leaking through the obscuring material.

Previous studies have found that between 1% and 4% of field galaxies show variability that could be associated with low-luminosity AGNs (Sarajedini et al. 2000). The effects of the emission produced by the accreting black hole on the spectrum and the images of the galaxies containing a low-luminosity AGN are rarely detectable. For example, broad emission lines are not present in the galaxy spectrum even if the AGN is not obscured as the AGN emission is heavily diluted by the host galaxy light. If there is an underlying low-luminosity AGN, a careful subtraction of two images of the galaxy may uncover the presence of a variable AGN (Sarajedini et al. 2000). Since in our survey we do not subtract a reference image from the rest of the images, a reliable identification of these low-luminosity AGNs is difficult. Given that our sample of galaxies is X-ray selected and some of them show narrow emission lines, the probability of finding a low-luminosity AGN is higher than for a sample of normal field galaxies. Among our sample of GALs, we found that 22% of them show variability and 8.7% show variability consistent with an accretion disk. In particular, XID
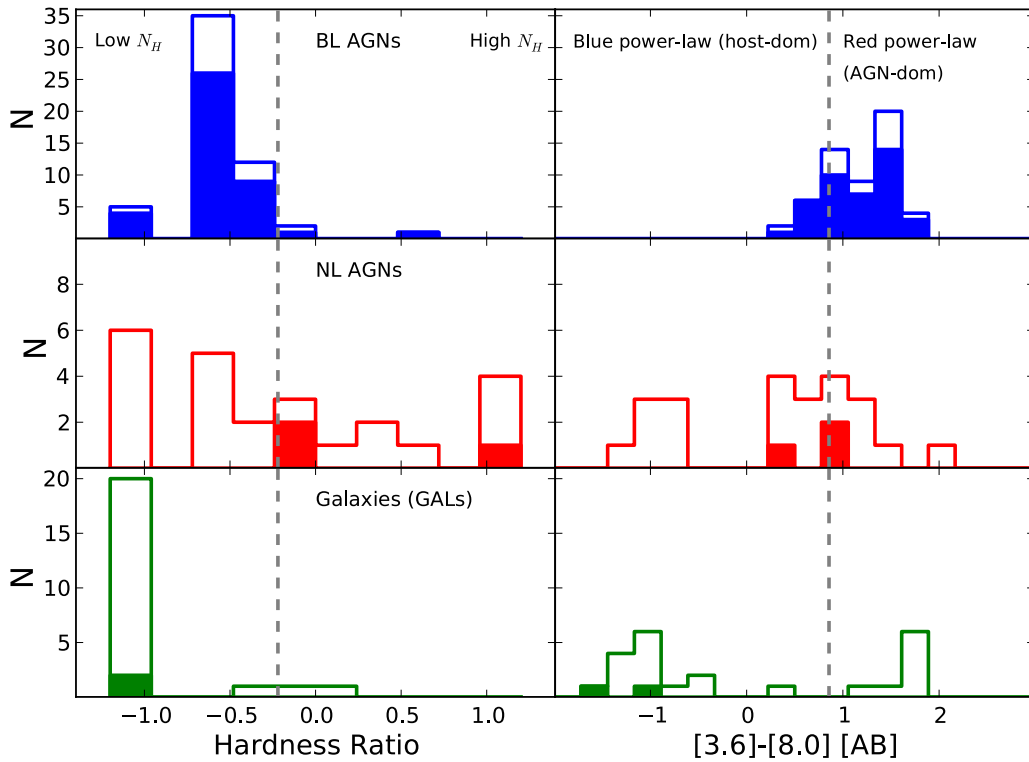
Figure 20. In the left panel we show the overall distribution (step-line histogram) of BL AGNs (top panel), NL AGNs (middle panel), and GAL ojects (bottom panel) as a function of the hardness ratio, while in the right panel we show the same distributions as a function of the [3.6]–[8.0] color. The distributions of variable sources are shown as shaded histograms in the panels. In the left panel the gray dashed line corresponds to HR = −0.2, the division between unobscured (low $N_{\rm H}$) and obscured (high $N_{\rm H}$) AGNs, and in the right panel the gray dashed line corresponds to the division between AGN-dominated and host-dominated sources of Brusa et al. (2010).

10569 is clearly variable (rms >0.05 mag) and consistent with the variation expected for an AGN.

8. DISCUSSION AND CONCLUSIONS

In this paper we present the characterization of the QUEST–La Silla AGN variability survey. The survey is a novel effort to obtain highly sampled optical light curves in well-studied extragalactic fields, making use of the QUEST camera at the ESO-Schmidt telescope at La Silla. Our observing strategy will provide good-quality light curves for many sources that already have a large data set of multiwavelength observations and will increase the number of AGN candidates in the areas of the survey where an AGN classification is missing or is based only on a color–color selection (Schmidt et al. 2010; Butler & Bloom 2011; Palanque-Delabrouille et al. 2011; Graham et al. 2014). Additionally, the survey is producing highly sampled light curves for all classes of interesting transients (see, e.g., Rabinowitz et al. 2012; Zinn et al. 2014; R. Cartier et al. 2015, in preparation).

In this paper, we showed that we are obtaining good astrometry, with an internal precision of ∼0″.1 and with an overall accuracy of 0″.2 compared to SDSS. In the future, the QSOs lying within our observing fields may be used as references to increase the internal astrometric precision of the survey.

We defined the Q band as the union of the g and r bands, and we showed that calibrating the Q band as an equivalent to the $(g + r)_{\rm SDSS}$ photometric system yields a photometric dispersion of ∼0.05 mag. Furthermore, we quote, conservatively, a systematic error in our zero point of 0.05 mag.

We found that the use of a linear model to fit the zero point as a function of the instrumental magnitude q produces a better calibration of our data, increasing significantly the number of non-variable stars and reducing the skewness in the $Q - (g + r)_{\rm SDSS}$ residuals as a function of Q.

We demonstrated that we are obtaining good photometry in the range $14.0 \lesssim Q \lesssim 19.5$. Since we are observing a minimum of two images per tile in a given night, we expect to produce light curves using nightly stacked images. Our preliminary results indicate that in the near future we will produce good-quality light curves with extraordinary cadence of observations to a magnitude limit of $Q \sim 20.5$ (roughly $r \sim 21$), or deeper.

As a way to explore the quality of the data collected by our survey, we studied the optical variability of X-ray XMM-COSMOS sources of Brusa et al. (2010). In this study, we found that the QUEST–La Silla AGN variability survey is ∼75%–80% complete in the XMM-COSMOS field to a magnitude limit of $r \sim 20$, and ∼67% complete to a magnitude of $r \sim 21$. Therefore, the survey loses roughly 20% of the objects, possibly owing to large defective areas, permanently or randomly off detectors, and gaps between detectors.

Based on the variability index V (see Section 7.2), we found that 80% ± 5% of the BL objects are classified as variable objects, while 21% ± 8% of the NL objects and 22% ± 9% of the GAL objects are classified as variable objects.

We studied the relation between $\sigma_{\rm rms}$ and the [3.6]–[8.0] mid-IR color and found that objects that are redder in the mid-IR (possibly AGN dominated) tend to show larger $\sigma_{\rm rms}$. A possible interpretation of this result is that the emission of the host galaxy dilutes AGN variability in objects that are more host
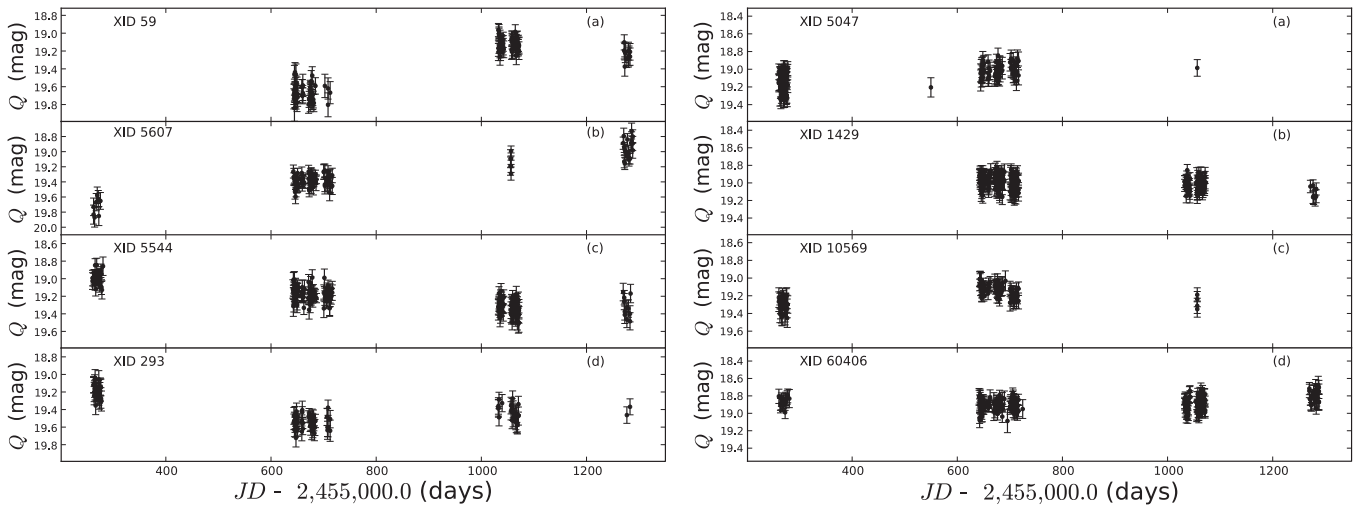
Figure 21. Q-band light curves of XMM-COSMOS variable objects. In the top right of each panel is the XMM-COSMOS identifier number for each object.

Table 6
Properties of Some of the Most Variable XMM-COSMOS Objects

Name	Class	z	r mag	$P_{\rm var}$[a]	$\sigma_{\rm rms}$	[3.6]–[8.0] AB Color	Host/AGN Dominated[b]	HR	Obscured/ Unobscured[c]
XID 59	BL	1.920	20.50	>0.999	0.258	1.41	AGN	−0.51	Unobscured
XID 5607	BL	1.359	20.52	>0.999	0.197	1.70	AGN	−1.00	Unobscured
XID 5544	BL	1.889	20.21	>0.999	0.108	1.54	AGN	−0.55	Unobscured
XID 293	NL	0.445	20.32	>0.999	0.137	0.93	AGN	−0.02	Obscured
XID 5047	NL	0.252	20.10	>0.999	0.068	0.25	Host	1.00	Obscured
XID 1429	NL	0.356	19.77	0.999	0.025	0.87	AGN	−0.20	Obscured
XID 10569	GAL	0.348	19.91	>0.999	0.067	−1.15	Host	−1.00	Unobscured
XID 60406	GAL	0.166	19.77	0.978	0.038	−1.54	Host	−1.00	Unobscured

Notes.
[a] We defined $P_{\rm var} = 1 - P(\chi^2)$ (see Section 7.2), interpreted as the probability of an object to be variable based on its χ^2 value and the number of observations.
[b] We used the division between AGN- and host-dominated sources of Brusa et al. (2010), which is based on the mid-IR color ([3.6]–[8.0]) of the source.
[c] We follow the convention that sources with HR < −0.2 are unobscured.

galaxy dominated. We also found that overall BL objects have larger variation amplitudes (e.g., higher $\sigma_{\rm rms}$) than NL and GAL objects. However, a significant fraction (∼33%) of NL variable objects show significant variability.

We studied the variability as a function of the time elapsed between observations (τ) in the best-observed sample using the "normalized" structure function (SF$_{\rm norm}$), i.e., after correction for measurement errors. We parameterized SF$_{\rm norm}(\tau)$ as a power law ($A\tau^\gamma$) and found that BL AGNs tend to be located in a region with large amplitudes ($A > 0.1$) and power-law exponents ($\gamma > 0.025$) compared to the bulk of NL AGNs and GALs. We also demonstrated that the variability in variable NL AGNs and GALs with $A > 0.1$ and $\gamma > 0.025$ seems to be the result of an accreting supermassive black hole as in the case of BL AGNs and not an artifact of the observations. We found that 74.5% of BL AGNs, 12.4% of NL AGNs, and 8.7% of GALs are variables and have $A > 0.1$ and $\gamma > 0.025$.

We confirm that the majority of the BL variable objects have mid-IR colors ([3.6]–[8.0]), consistent with being AGN dominated, and HRs consistent with unobscured X-ray sources. On the other hand, we found that although 54% ±10% of the NL objects in the best-observed sample are unobscured according to the HR division, 100% of the NL AGNs showing variability consistent with being powered by a supermassive black hole ($V > 1.3$, $\gamma > 0.025$, and $A > 0.1$) are obscured. This is an

interesting result that requires confirmation from larger samples with high-quality light curves. The time span of our QUEST–La Silla light curves will continue to increase until 2016, so we expect to revisit this result in a future paper.

The [3.6]–[8.0] mid-IR color distribution of NL objects shows a large spread, with a group of NL objects showing very blue colors and a second group with redder colors peaking close to the division between AGN-dominated and host-dominated sources of Brusa et al. (2010), but located on the blue side of the BL distribution (see Figure 20).

Although the NL AGN sample is small, we noticed that the objects with larger excess variance and with $\gamma > 0.025$ and $A > 0.1$ are those with relatively red mid-IR colors and larger values of HR (see Figure 17). Thus, a possible interpretation of variable NL objects is that they are obscured sources, in which the optical variability could be the result of leaked or scattered disk emission. However, an increase of the sample size is definitely required to have conclusive interpretations.

GALs show a large spread in their [3.6]–[8.0] color distribution. However, all variable GAL sources have blue mid-IR colors and thus are consistent with being host-dominated objects. Additionally, assuming that variable GALs with $\gamma > 0.025$ and $A > 0.1$ contain an AGN, we find that these are unobscured X-ray sources according to the HR definition. Consequently, a plausible interpretation for the

variable GAL objects having $\gamma > 0.025$ and $A > 0.1$ is that they are low-luminosity AGNs.

REFERENCES

Abazajian, K. N., Adelman-McCarthy, J. K., Agüeros, M. A., et al. 2009, ApJS, 182, 543
Abbott, T., Aldering, G., Annis, J., et al. (The Dark Energy Survey Collaboration) 2005, arXiv:astro-ph/0510346
Adelman-McCarthy, J. K., Agüeros, M. A., Allam, S. S., et al. 2006, ApJS, 162, 38
Ai, Y. L., Yuan, W., Zhou, H. Y., et al. 2010, ApJL, 716, L31
Arévalo, P., Uttley, P., Kaspi, S., et al. 2008, MNRAS, 389, 1479
Arévalo, P., Uttley, P., Lira, P., et al. 2009, MNRAS, 397, 2004
Assef, R. J., Stern, D., Kochanek, C. S., et al. 2013, ApJ, 772, 26
Baltay, C., Rabinowitz, D., Andrews, P., et al. 2007, PASP, 119, 1278
Bertin, E. 2006, in ASP Conf. Ser. 351, Astronomical Data Analysis Software and Systems XV, ed. C. Gabriel et al. (San Francisco, CA: ASP), 112
Bertin, E., & Arnouts, S. 1996, A&A, 117, 393
Brusa, M., Civano, F., Comastri, A., et al. 2010, ApJ, 716, 348
Butler, N. R., & Bloom, J. S. 2011, AJ, 141, 93
Capak, P., Aussel, H., Ajiki, M., et al. 2007, ApJS, 172, 99
Collier, A., & Peterson, B. M. 2001, ApJ, 555, 775
Cristiani, S., Trentini, S., La Franca, F., & Andreani, P. 1997, A&A, 321, 123
Drake, A. J., Djorgovski, S. G., Mahabal, A., et al. 2009, ApJ, 696, 870
Elvis, M., Civano, F., Vignali, C., et al. 2009, ApJS, 184, 158
Fan, X. 1999, AJ, 117, 2528
Frieman, J., Bassett, B., Becker, A., et al. 2008, AJ, 135, 338
Gierliński, M., Nikolajuk, M., & Czerny, B. 2008, MNRAS, 383, 741
Graham, M. J., Djorgovski, S. G., Drake, A. J., et al. 2014, MNRAS, 439, 703
Hamuy, M., Suntzeff, N. B., Heathcote, S. R., et al. 1994, PASP, 106, 566
Hamuy, M., Walker, A. R., Suntzeff, N. B., et al. 1992, PASP, 104, 533
Hasinger, G. 2008, A&A, 490, 905
Hodapp, K. W., Kaiser, N., Aussel, H., et al. 2004, AN, 325, 63
Hook, I. M., McMahon, R. G., Boyle, B. J., & Irwin, M. J. 1994, MNRAS, 268, 305
Ilbert, O., Capak, P., Salvato, M., et al. 2009, ApJ, 690, 1236
Ivezić, Z., Smith, J. A., Miknaitis, G., et al. 2007, AJ, 134, 973
Ivezić, Z., Tyson, J. A., Acosta, E., et al. (LSST Collaboration) 2008, arXiv:0805.2366
Jarvis, M. J., Bonfield, D. G., Bruce, V. A., et al. 2013, MNRAS, 428, 1281
Kauffmann, G., Heckman, T. M., Tremonti, C., et al. 2003, MNRAS, 346, 1055
Kelly, B. C., Bechtold, J., & Siemiginowska, A. 2009, ApJ, 698, 895
Kelly, B. C., Treu, T., Malkan, M., Pancoast, A., & Woo, J. 2013, ApJ, 778, 187
Kim, D.-W., Protopapas, P., Trichas, M., et al. 2012, ApJ, 747, 107
Kozłowski, S., & Kochanek, C. S. 2009, ApJ, 710, 508
Kozłowski, S., Kochanek, C. S., Udalski, A., et al. 2010, ApJ, 708, 927
Lacy, M., Storrie-Lombardi, L. J., Sajina, A., et al. 2004, ApJS, 154, 166
Lang, D., Hogg, D. W., Mierle, K., Blanton, M., & Roweis, S. 2010, ApJ, 139, 1782
Lanzuisi, G., Ponti, G., Salvato, M., et al. 2014, ApJ, 781, 105
Law, N. M., Kulkarni, S. R., Dekany, R. G., et al. 2009, PASP, 121, 1395
Le Floc'h, E., Aussel, H., Ilbert, O., et al. 2009, ApJ, 703, 222
Lilly, S. J., Le Brun, V., Maier, C., et al. 2009, ApJS, 184, 218
Lilly, S. J., Le Fèvre, O., Renzini, A., et al. 2007, ApJS, 172, 70
Lira, P., Arévalo, P., Uttley, P., McHardy, I., & Breedt, E. 2011, MNRAS, 415, 1209
Lira, P., Arévalo, P., Uttley, P., McHardy, I. M. M., & Videla, L. 2015, MNRAS, submitted
Lira, P., Videla, L., Wu, Y., et al. 2013, ApJ, 764, 159
MacLeod, C. L., Books, K., Ivezić, Z., et al. 2011, ApJ, 728, 26
MacLeod, C. L., Ivezić, Z., Kochanek, C. S., et al. 2010, ApJ, 721, 1014
Mainieri, V., Hasinger, G., Cappelluti, N., et al. 2007, ApJS, 172, 368
McCracken, H. J., Capak, P., Salvato, M., et al. 2010, ApJ, 708, 202
McCracken, H. J., Milvang-Jensen, B., Dunlop, J., et al. 2012, A&A, 544, 156
McHardy, I. M. 1988, MmSAI, 59, 239
McHardy, I. M. 2013, MNRAS, 430, L49
McHardy, I. M., Koerding, E., Knigge, C., Uttley, P., & Fender, R. P. 2006, Natur, 444, 730
McLaughlin, M. A., Mattox, J. R., Cordes, J. M., & Thompson, D. J. 1996, ApJ, 473, 763
Meusinger, H., & Weiss, V. 2013, A&A, 506, 104
Monet, D. G., Levine, S. E., Canzian, B., et al. 2003, AJ, 125, 984
Mor, R., & Netzer, H. 2012, MNRAS, 420, 526
Morganson, E., Burgett, W. S., Chambers, K. C., et al. 2014, ApJ, 784, 92
Palanque-Delabrouille, N., Yeche, Ch., Myers, A. D., et al. 2011, A&A, 530, 122
Paolillo, M., Schreier, E. J., Giacconi, R., Koekemoer, A. M., & Grogin, N. A. 2004, ApJ, 611, 93
Polletta, M., Tajer, M., Maraschi, L., et al. 2007, ApJ, 663, 81
Prescott, M. K. M., Impey, C. D., Cool, R. J., & Scoville, N. Z. 2006, ApJ, 644, 100
Rabinowitz, D., Schwamb, W. E., Hadjiyska, E., & Tourtellotte, S. 2012, AJ, 144, 140
Rau, A., Kulkarni, S. R., Law, N. M., et al. 2009, PASP, 121, 1334
Richards, G. T., Fan, X., Newberg, H. J., et al. 2002, AJ, 123, 2945
Richards, G. T., Myers, A. D., Gray, A. G., et al. 2009, ApJS, 180, 67
Sanders, D. B., Salvato, M., Aussel, H., et al. 2007, ApJS, 172, 86
Sarajedini, V. L., Gilliland, R. L., & Phillips, M. M. 2000, AJ, 120, 2825
Schlegel, D. J., Finkbeiner, D. P., & Davis, M. 1998, ApJ, 500, 525
Schmidt, K. B., Marshall, P. J., Rix, H.-W., et al. 2010, ApJ, 714, 1194
Schmidt, M., & Green, R. F. 1983, ApJ, 269, 352
Sesar, B., Ivezić, Z., Lupton, R. H., et al. 2007, AJ, 134, 2236
Shemmer, O., Brandt, W. N., Paolillo, M., et al. 2014, ApJ, 783, 116
Stern, D., Eisenhardt, P., Gorjian, V., et al. 2005, ApJ, 631, 163
Stetson, P. B. 1987, PASP, 99, 191

Tonry, J. L., Stubbs, C. W., Lykke, K. R., et al. 2012, ApJ, 750, 99
Trevese, D., Kron, R. G., Majewski, S. R., Bershady, M. A., & Koo, D. C. 1994, ApJ, 433, 494
Trump, J. R., Impey, C. D., Elvis, M., et al. 2009, ApJ, 696, 1195
Trump, J. R., Impey, C. D., McCarthy, P. J., et al. 2007, ApJS, 172, 383
Uomoto, A. K., Wills, B. J., & Wills, D. 1976, AJ, 81, 905
Vanden Berk, D. A., Richards, G. T., Bauer, A., et al. 2001, AJ, 122, 549
Vanden Berk, D. A., Wilhite, B. C., Kron, R. G., et al. 2004, ApJ, 601, 692
Wilhite, B. C., Brunner, R. J., Grier, C. J., Schneider, D. P., & Vanden Berk, D. E. 2008, MNRAS, 383, 1232
Wold, M., Brotheron, M. S., & Shang, Z. 2007, MNRAS, 375, 989
York, D. G., Adelman, J., Anderson, J. E., et al. 2000, AJ, 120, 1579
Zinn, R., Horowitz, B., Vivas, A. K., et al. 2014, ApJ, 781, 22
Zuo, W., Wu, X.-B., Liu, Y.-Q., & Jiao, C.-L. 2012, ApJ, 758, 104